


# Fixed points as regulatory hubs in discrete memristive neural networks: An analysis of the FitzHugh-Nagumo model

Shaobo He(贺少波), Jiawei Xiao(肖佳伟), Qilai Chen(陈祺来), and Huihai Wang(王会海)
**Citation:**Chin. Phys. B, 2026, 35 (**6**): 060502. DOI: 10.1088/1674-1056/ae3131
http://cpb.iphy.ac.cn; http://iopscience.iop.org/cpb

**What follows is a list of articles you may be interested in**

---

## Dynamics analysis and DSP implementation of the Rulkov neuron model with memristive synaptic crosstalk

Yichen Bi(毕毅晨), Jun Mou(牟俊), Herbert Ho-Ching Iu, Nanrun Zhou(周南润), Santo Banerjee, and Suo Gao(高锁)
Chin. Phys. B, 2026, 35 (**1**): 010504. DOI: 10.1088/1674-1056/ae1728

## Dynamical behavior of ring-star neural networks with small-world characteristics

Minglin Ma(马铭磷), Zhiyi Yuan(袁芷依), Umme Kalsoom, Weizheng Deng(邓为政), and Shaobo He(贺少波)
Chin. Phys. B, 2025, 34 (**10**): 100502. DOI: 10.1088/1674-1056/adde39

## A novel non-autonomous hyperchaotic map based on discrete memristor parallel connection

Weiping Wu(吴伟平), Mengjiao Wang(王梦蛟), and Qigui Yang(杨启贵)
Chin. Phys. B, 2025, 34 (**5**): 050503. DOI: 10.1088/1674-1056/adb8bc

## A novel hyperchaotic map with sine chaotification and discrete memristor

Qiankun Sun(孙乾坤), Shaobo He(贺少波), Kehui Sun(孙克辉), and Huihai Wang(王会海)
Chin. Phys. B, 2022, 31 (**12**): 120501. DOI: 10.1088/1674-1056/ac8f3a

## The dynamics of a memristor-based Rulkov neuron with fractional-order difference

Yan-Mei Lu(卢艳梅), Chun-Hua Wang(王春华), Quan-Li Deng(邓全利), and Cong Xu(徐聪)
Chin. Phys. B, 2022, 31 (**6**): 060502. DOI: 10.1088/1674-1056/ac539a

---

**SPECIAL TOPIC — Biophysical circuits: Modeling & applications in neuroscience**

# Fixed points as regulatory hubs in discrete memristive neural networks: An analysis of the FitzHugh–Nagumo model

Shaobo He(贺少波)[1], Jiawei Xiao(肖佳伟)[1], Qilai Chen(陈祺来)[1,†], and Huihai Wang(王会海)[2]

[1] *School of Automation and Electronic Information, Xiangtan University, Xiangtan* 411105, *China*
[2] *School of Physics and Electronics, Central South University, Changsha* 410083, *China*

(Received 29 September 2025; revised manuscript received 24 December 2025; accepted manuscript online 26 December 2025)

This study investigates the dynamics of discrete memristive FitzHugh–Nagumo (FHN) neural networks. We introduce a discrete memristor with hyperbolic tangent nonlinearity and incorporate it into neuron models ranging from single neurons and coupled pairs to complex networks with ring and small-world topologies. Stability and bifurcation analyses reveal transitions from periodic to chaotic dynamics. A key contribution is the identification of a constant fixed point that remains invariant across periodic, weakly chaotic, and chaotic regimes. Linear stability analysis of this fixed point provides a fundamental basis for understanding the system's dynamical evolution. The fixed point theory explains how memristive coupling induces diverse synchronization patterns, including stable phase-locking and synchronization–desynchronization transitions, and further accounts for the emergence of chimera states in ring networks as well as their alteration in small-world networks owing to long-range connections. Field-programmable gate array (FPGA) implementation successfully validates the mathematical models, confirming the feasibility of hardware realization. Overall, this work establishes a theoretical framework linking fixed point properties with firing mechanisms and synchronization dynamics in discrete memristive FHN neural networks, providing insights into potential applications in neuromorphic computing.

**Keywords:** discrete memristor, discrete neuron, complex network, chimera state, FPGA implementation

**PACS:** 05.45.–a, 84.30.–r, 89.75.–k, 07.05.–t

**DOI:** 10.1088/1674-1056/ae3131 **CSTR:** 32038.14.CPB.ae3131

## 1. Introduction

Recently, memristors have attracted considerable interest from the scientific community, primarily due to their groundbreaking potential applications in neuromorphic computing and next-generation memory apparatus.[1,2] Beyond these applications, their unique characteristics have also established them as a fundamental building block for constructing and studying complex nonlinear dynamic systems.[3] The theoretical foundation of this circuit element was first established by Chua in 1971, who postulated it as the fourth fundamental circuit element characterized by a dynamic relationship between charge and flux. This seminal concept has since been expanded through the rigorous mathematical modeling of memristive systems.[4] In contrast to conventional resistors, memristors exhibit a distinctive property: their resistance is contingent upon the historical profile of the applied voltage and current, a feature known as the "pinched hysteresis loop". This non-volatile memory effect is the key mechanism that enables them to effectively emulate synaptic plasticity within artificial neural networks.[5,6] Specifically, the dynamic adjustment of memristance can mimic the strengthening or weakening of synapses, which has been successfully demonstrated in various models of artificial neural networks to achieve learning and adaptive capabilities.[7,8]

A key model in neuroscience and nonlinear dynamics is the FitzHugh–Nagumo (FHN) model, developed independently by FitzHugh and Nagumo in the early 1960s as a simplified alternative to the classical Hodgkin–Huxley (HH) model.[9] FitzHugh's 1961 work[10] introduced a two-variable system that captures the essential excitability properties of nerve membranes — including action potential generation and refractory periods — while drastically reducing the computational complexity of the original HH framework, which relied on four variables to describe ion channel dynamics. This simplification was further refined by Nagumo and colleagues,[11] who demonstrated the model's capability to simulate pulse transmission along nerve axons, thereby validating its ability to reproduce biological signal propagation with remarkable accuracy.

The enduring significance of the FHN model lies in its balance between biological realism and mathematical tractability. Unlike the HH equations, which require solving complex sets of nonlinear differential equations, the FHN model uses a pair of coupled equations to describe membrane potential dynamics and recovery processes. This simplicity has enabled its widespread application across diverse fields: from studying neuronal excitability and synchronization in neural networks to modeling cardiac rhythms and de-

†Corresponding author. E-mail: chenqilai277@xtu.edu.cn

© 2026 Chinese Physical Society and IOP Publishing Ltd. All rights, including for text and data mining, AI training, and similar technologies, are reserved.

signing artificial excitable systems. Recent extensions have incorporated more complex dynamics, particularly through the integration of memristors, which introduce memory effects and rich nonlinearity. This has led to the exploration of advanced systems such as fractional-order memristive hyperchaotic systems,[12] while He *et al.*[13] contributed to the modeling of discrete fractional memristors, thereby expanding the mathematical framework for such systems and further broadening the relevance of FHN-based models to contemporary nonlinear research.

The introduction of memristive synapses into the FHN model has opened new avenues for studying complex neural dynamics. The seminal work by Muthuswamy and Chua[14] on simple chaotic circuits paved the way for understanding nonlinear dynamics in memristive systems. Subsequent research by You *et al.*[15] further demonstrated the emergence of chaotic dynamics in memristor-based FHN neuron models.

The integration of memristors into discrete dynamical systems has concurrently emerged as a prominent research direction, particularly in engineering applications.[16] Discrete memristive neural networks exhibit rich nonlinear behaviors, making them suitable for applications in secure communication,[17] intelligent signal processing,[18] and brain-inspired computing.[19] These systems demonstrate remarkable properties such as multistability and hidden attractors, which have been extensively studied in various memristive circuits and systems.[20]

Memristors introduce essential nonlinear dynamics into neural networks, leading to complex behaviors such as multistability, chaotic attractors, and bifurcation phenomena.[21,22] The stability and bifurcation analysis in memristor-based neural networks has been thoroughly investigated by Xiao *et al.*,[23] providing important theoretical foundations for the field. Additionally, research on synchronization aspects has revealed how memristive neural networks with time-varying delays can achieve adaptive synchronization.[24]

These properties have been leveraged to enhance memory retention and synaptic learning in artificial neural networks. Moreover, the hysteresis characteristic of memristors enables energy-efficient neuromorphic computing, offering an alternative to conventional von Neumann architectures. The complex dynamics of memristor-based neural networks and their potential for advanced computing applications have been further demonstrated in various studies.[25]

While continuous-time FHN models have been extensively studied, their discrete counterparts have received less attention. However, discrete models provide significant computational advantages for digital signal processing and hardware implementation. Furthermore, the discrete FHN model significantly extends classical neural models by incorporating memristive synapses. This integration introduces novel nonlinearities and memory effects, leading to complex dynamical behaviors — including multistability and chaos — that necessitate rigorous mathematical analysis,[26] particularly in the context of their applications to neuromorphic computing.[27]

The collective behavior of neural networks, a canonical example of complex systems, emerges from nonlinear interactions between neurons. Of particular interest are the synchronization phenomena and diverse oscillatory patterns that arise from local synaptic coupling. The network topology, such as ring or small-world structures, plays a crucial role in shaping these global dynamics. For instance, Ma *et al.*[28] recently constructed a ring-star neural network with small-world characteristics, demonstrating how the strengths of ring and star coupling non-monotonically regulate network synchronization behavior, thereby highlighting the critical role of network topology in synchronization dynamics.

Recent studies have further expanded our understanding of memristive neural networks. Ma *et al.*[29] reported synchronization coexistence in Rulkov neural networks based on locally active discrete memristors, while Lu *et al.*[30] systematically investigated dynamical behaviors in discrete memristor-coupled small-world neuronal networks. Concurrently, Wu *et al.*[31] developed a novel non-autonomous hyperchaotic map based on discrete memristor parallel connection. These recent advances motivate the present investigation of the FHN model with discrete memristive synapses, with particular emphasis on establishing a unified fixed point theory.

In memristive neural networks, fixed points provide fundamental insight into the stability and global organization of their collective dynamics. Since memristive coupling introduces state-dependent nonlinearity, characterizing fixed points helps identify controllable dynamical regimes, enabling reliable oscillation suppression or synchronization regulation in neuromorphic systems. Recent studies have emphasized the role of equilibrium analysis in determining stability boundaries and transition routes in neuron networks.[32,33]

In this context, introducing memristive synapses adds another layer of complexity due to their history-dependent properties, often leading to richer behaviors such as multistability and chaos. These phenomena are the focus of this work.

Memristive neural networks introduce additional nonlinear degrees of freedom due to their history-dependent resistance characteristics, leading to substantially richer dynamical behaviors compared to traditional neural models. This enhanced complexity is evident in both analog implementations, where circuit realizations of discrete-time memristor models demonstrate unique switching dynamics,[34] and in memristor-based spiking neuron models, which provide novel insights into neural coding strategies and information processing mechanisms,[35] offering more biologically plausible implementations of neural computation.

The interplay between chaotic dynamics and synchronization in memristive FHN networks represents a particularly active research frontier. Previous investigations have revealed that memristive coupling can induce complex synchronization patterns, including complete synchronization in identical systems and phase synchronization in non-identical counterparts.[36] These systems also exhibit remarkable phenomena such as multistability, where multiple stable states coexist under identical parameter conditions, and intricate bifurcation scenarios that govern transitions between different dynamical regimes.[37] The emerging patterns include phase synchronization, anti-synchronization, and even chimera states[38] where synchronized and desynchronized populations coexist in coupled neuron models.

These complex dynamical properties are crucial for understanding biological information processing mechanisms, where controlled synchronization and desynchronization play fundamental roles in cognitive functions such as perceptual integration, attentional modulation, and memory formation processes.[39] The nonlinear dynamics of memristive neural networks not only provide insights into neural computation principles but also enable novel computing paradigms that leverage their inherent memory and adaptive capabilities for neuromorphic applications.[40]

To characterize the complex dynamical behavior of memristive FHN networks, we use a comprehensive analytical framework that combines Lyapunov exponent (LE) analysis and bifurcation theory. LEs provide crucial insights into system stability and the rate of trajectory divergence or convergence in phase space,[41] while bifurcation diagrams reveal intricate transitions between periodic oscillations and chaotic states under parameter variations.[42] The investigation of synchronization phenomena, particularly in discrete-time memristive neural networks with time delays, offers additional insights into the temporal coordination of complex neural dynamics.[43]

The presence of multistability and coexisting attractors in memristive systems further underscores their relevance in modeling real-world neural dynamics. These complex dynamical features, including chaos and bifurcation patterns, have been extensively observed in novel discrete memristor-based neuronal models,[44] highlighting the rich behavioral repertoire that emerges from the interplay between memristive properties and neural dynamics.

The present study focuses on the design and analytical examination of a discrete memristive FHN network, investigating its stability characteristics, bifurcation configurations, and chaotic dynamical behaviors. The research establishes connections between memristive electronics, nonlinear dynamical systems, and neural network theories, providing a theoretical framework and hardware validation for future bio-inspired computational systems. The primary contributions, detailed in subsequent sections, include:

(i) Mathematical formulation of the discrete memristive FHN network with memristor-based nonlinearities.

(ii) Stability and bifurcation analysis to identify conditions for periodic and chaotic behaviors.

(iii) Proposal and proof of the fixed point concept for the network's motion trajectories.

(iv) Verification of chimera states in complex networks with different topologies.

(v) Field-programmable gate array (FPGA) implementation validating the mathematical models.

The subsequent content is organized as follows: Section 2 presents the mathematical formulation of the discrete memristive FHN network. Section 3 designs networks ranging from single neurons to complex topologies. Section 4 explores stability conditions, bifurcation structures, LE analysis, fixed point theory, and synchronization dynamics. Section 5 details the FPGA implementation and hardware validation. Section 6 provides concluding remarks.

## 2. Models of the discrete memristor and neuron

This section introduces models of the discrete memristor and the discrete FHN neuron. Numerical simulations are conducted to elucidate the rich dynamical behaviors exhibited by these models.

### 2.1. The model of discrete memristors

Based on the difference operator, the discrete memristor[12] can be defined by

$$\begin{cases} v(t_n) = M(\varphi(t_n)) \cdot i(t_n), \\ \Delta\varphi(t_n) = \kappa \cdot i(t_n), \end{cases} \tag{1}$$

where $\varphi(t_n)$ is the internal state variable of the discrete memristor, $i(t_n)$ is the input signal, $v(t_n)$ is the output signal, $\kappa$ is a rate parameter, $\Delta\varphi(t_n) = \varphi(t_{n+1}) - \varphi(t_n)$ is the forward difference, and $M(\cdot)$ is the memristance function.

According to the definition of $\Delta\varphi(t_n)$, we have

$$\begin{cases} \varphi(t_1) - \varphi(t_0) = \kappa \cdot i(t_0), \\ \varphi(t_2) - \varphi(t_1) = \kappa \cdot i(t_1), \\ \vdots \\ \varphi(t_{n+1}) - \varphi(t_n) = \kappa \cdot i(t_n), \end{cases} \tag{2}$$

where $n = 0, 1, 2, \ldots$.

Summing both sides yields the cumulative relation

$$\varphi(t_{n+1}) = \varphi(t_0) + \kappa \sum_{j=0}^{n} i(t_j). \tag{3}$$

The system can be further expressed as

$$\varphi(t_{n+1}) = \varphi(t_0) + \kappa \sum_{j=0}^{n} i(t_j)$$

$$= \varphi(t_0) + \kappa \sum_{j=0}^{n-1} i(t_j) + \kappa i(t_n) = \varphi(t_n) + \kappa i(t_n). \quad (4)$$

Therefore, the discrete memristor can generally be described as

$$\begin{cases} v(t_n) = M(\varphi(t_n)) \cdot i(t_n), \\ \varphi(t_{n+1}) = \varphi(t_n) + \kappa \cdot i(t_n). \end{cases} \quad (5)$$

The above definition of a discrete memristor is established from a mathematical perspective based on the sampling principle in circuits. We assume that the discrete memristor characterizes the relationship between discrete-time input and output signals.

Specifically, in this paper, a discrete memristor with hyperbolic tangent nonlinearity is introduced and defined as

$$\begin{cases} v(t_n) = \phi \cdot \tanh(\varphi(t_n)) \cdot i(t_n), \\ \varphi(t_{n+1}) = \varphi(t_n) + \kappa \cdot i(t_n), \end{cases} \quad (6)$$

where $\phi$ denotes the amplitude of the nonlinearity.

This choice of hyperbolic tangent nonlinearity is motivated by its boundedness and smoothness, which ensure numerical stability in discrete-time simulations and provide a biologically plausible representation of synaptic saturation effects.[45,46]

Although the discrete memristor is constructed using the discrete difference operator, it is also instructive to establish its correspondence with a continuous memristor model. The corresponding continuous memristor is defined as

$$\begin{cases} v(t) = \phi \cdot \tanh(\varphi(t)) \cdot i(t), \\ \dfrac{\mathrm{d}\varphi(t)}{\mathrm{d}t} = \eta \cdot i(t), \end{cases} \quad (7)$$

where $v(t)$ and $i(t)$ denote the terminal voltage and current, respectively.

The internal state variable $\varphi(t)$ is proportional to the charge $q(t)$ that has passed through the device, i.e., $\varphi(t) = \eta \int i(t)\,\mathrm{d}t = \eta q(t)$. Here, $\phi$ scales the memristance and $\eta$ is a scaling factor. This continuous definition preserves the fundamental $v$–$i$ relationship of a memristive system.

To integrate this memristor into discrete neurons, Eq. (7) is discretized using the forward Euler method with time step $\Delta t$

$$\begin{cases} v(t_n) = \phi \cdot \tanh(\varphi(t_n)) \cdot i(t_n), \\ \varphi(t_{n+1}) = \varphi(t_n) + \eta \cdot \Delta t \cdot i(t_n). \end{cases} \quad (8)$$

Let $\kappa = \eta \Delta t$. Then Eq. (8) reduces to the discrete memristor model defined by Eq. (6). Throughout this work, we adopt $\kappa = 1$.

The Simulink model of the proposed discrete memristor is presented in Fig. 1. Let $\phi = 1$ and $i(t_n) = A\sin(\omega \pi t_n)$. When $A = 0.001$ and $\omega = 0.001$, 0.01, and 0.1, the corresponding hysteresis loops are shown in Fig. 2(a). It can be observed that the loop area decreases as the frequency $\omega$ increases. Furthermore, when $\phi = 1$ and $\omega = 0.001$, the hysteresis loops corresponding to $A = 0.001$, 0.005, and 0.01 are shown in Fig. 2(b).

Therefore, the proposed discrete memristor exhibits the characteristic pinched hysteresis loops and is consistent with the definition of a generalized memristor.

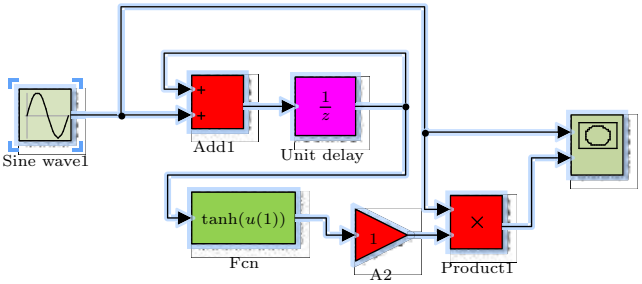



**Fig. 1.** Simulink model of the discrete memristor.

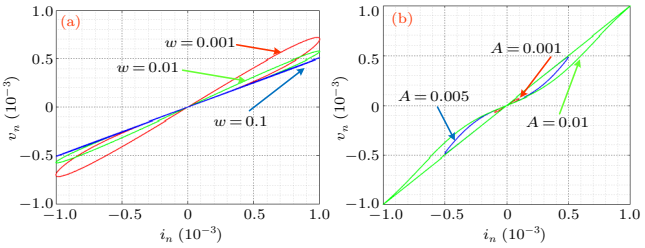



**Fig. 2.** Pinched hysteresis loops: (a) $\omega = 0.001$, 0.01, 0.1; and (b) $A = 0.001$, 0.005, 0.01.

To illustrate the numerical simulation procedure of the tanh-type discrete memristor, we present the implementation pseudocode in Algorithm 1. The primary function of this algorithm is to translate the mathematical model of the memristor into computable discrete steps, thereby enabling simulation of its dynamic response under input excitation. Using this pseudocode, the dynamic characteristics of the memristor can be accurately reproduced and analyzed.

**Algorithm 1** Pseudo code for realizing the memristor.

**Input:** $I, A, m_0$.
**Output:** $q(n), V(n)$.
$K \leftarrow \text{length}(I)$;
$q \leftarrow \text{zeros}(1, K)$;
$V \leftarrow \text{zeros}(1, K)$;
**for** $n = 1$ to $K$ **do**
    $m_0 \leftarrow m_0 + I(n)$;
    $q(n) \leftarrow m_0$;
    $V(n) \leftarrow A * \tanh(q(n)) * I(n)$;
**end for**

### 2.2. The discrete FHN neuron

The FHN model is a well-established mathematical model in neuroscience and serves as a simplified version of the HH model, capturing spiking behavior in neuronal electrical currents. The continuous-time FHN model is expressed

as

$$\begin{cases} \dfrac{\mathrm{d}x}{\mathrm{d}t} = x - \dfrac{1}{3}x^3 - y + I_{\mathrm{ext}}, \\ \dfrac{\mathrm{d}y}{\mathrm{d}t} = \varepsilon\left(x + \dfrac{b}{a} - \dfrac{1}{a}y\right), \end{cases} \tag{9}$$

where $x$ denotes the membrane potential (action potential), and $y$ is a recovery variable that modulates $x$. $I_{\mathrm{ext}}$ represents external excitation, while $a$ and $b$ are control parameters. Since the parameter $\varepsilon$ multiplies all terms on the right-hand side of the second equation, $y$ evolves more slowly than $x$. Both variables are dimensionless, with scaling relations $x = (V - V_0)/V_{\mathrm{s}}$ and $y = (W - W_0)/W_{\mathrm{s}}$, where $V$ and $W$ are physical quantities, $V_0$ and $W_0$ are reference values, and $V_{\mathrm{s}}$ and $W_{\mathrm{s}}$ are scaling factors.

Applying the forward Euler method, the system is discretized as

$$\begin{cases} x(t_{n+1}) = x(t_n) + h\left(x(t_n) - \dfrac{1}{3}x(t_n)^3 - y(t_n) + I_{\mathrm{ext}}\right) \\ \qquad\quad = (1+h)x(t_n) + h\left(-\dfrac{1}{3}x(t_n)^3 - y(t_n) + I_{\mathrm{ext}}\right) \\ \qquad\quad = \alpha_{11}x(t_n) + \alpha_{12}\left(-\dfrac{1}{3}x(t_n)^3 - y(t_n) + I_{\mathrm{ext}}\right), \\ y(t_{n+1}) = y(t_n) + h\varepsilon\left(x(t_n) - \dfrac{1}{a}y(t_n) + \dfrac{b}{a}\right) \\ \qquad\quad = \left(1 - \dfrac{h\varepsilon}{a}\right)y(t_n) + \dfrac{h\varepsilon}{a}\left(ax(t_n) + b\right) \\ \qquad\quad = \alpha_{21}y(t_n) + \alpha_{22}\left(ax(t_n) + b\right), \end{cases} \tag{10}$$

where $\alpha_{ij}$ are adjustment coefficients. The forward Euler method ensures numerical stability and aligns with recent studies on discretization of nonlinear neuronal dynamics.[47]

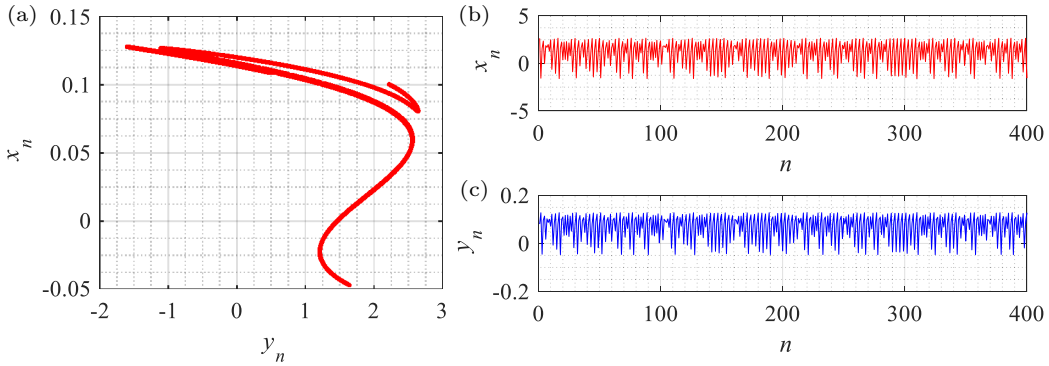



**Fig. 3.** Phase portrait of the discrete FHN neuron for $a = 0.4$, $b = 0.3$, and $I_{\mathrm{ext}} = 2.0$.

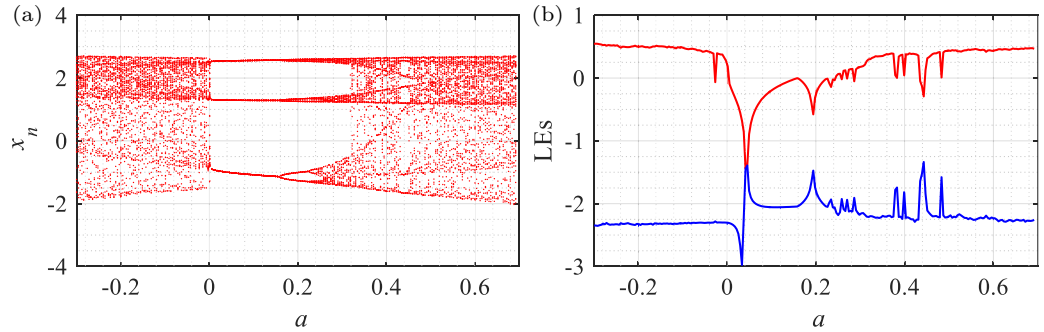



**Fig. 4.** (a) Bifurcation diagram and (b) LEs of disFHN with the system parameter $a$ varying and $k = 0.01$, $b = 0.3$, $I_{\mathrm{ext}} = 2.0$.

When $\alpha_{11} = 1$, $\alpha_{12} = 1$, $\alpha_{21} = -0.1$, and $\alpha_{22} = 0.1$, the system reduces to a generalized discrete FHN neuron model[48]

$$\begin{cases} x_{n+1} = x_n - \dfrac{1}{3}x_n^3 - y_n + I_{\mathrm{ext}}, \\ y_{n+1} = 0.1\left(ax_n + b\right) - 0.1y_n. \end{cases} \tag{11}$$

Here, parameter $a$ modulates the nonlinear interaction strength within the neuron, influencing the amplitude and frequency of action potential oscillations, while $b$ serves as a bias term affecting the baseline state and range of potential changes. Similar to the continuous model, the state variables and parameters in the discrete model are dimensionless and obtained via scaling.

## 3. Design of discrete memristive FHN network

### 3.1. FHN with one memristor

By introducing a memristor into the neuron, the mathematical model of the FHN with one memristor is given by

$$\begin{cases} x_{n+1} = x_n - \dfrac{1}{3}x_n^3 - y_n, \\ \qquad + I_{\mathrm{ext}} + k \cdot \tanh\left(\varphi_n\right)\left(x_n - x_{n-1}\right), \\ y_{n+1} = 0.1\left(ax_n + b\right) - 0.1y_n, \\ \varphi_{n+1} = \varphi_n + \kappa \cdot \left(x_n - x_{n-1}\right), \end{cases} \tag{12}$$

where $x_n - x_{n-1}$ represents the input to the discrete memristor, and $k$ is the coupling strength. The diagrammatic figure of this model is shown in Fig. 5.

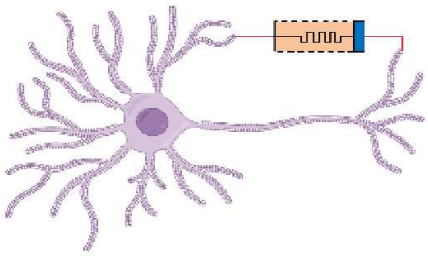


**Fig. 5.** The neuron with one memristor.

Let $w_{n+1} = x_n$, then the system can be redefined as

$$\begin{cases} x_{n+1} = x_n - \dfrac{1}{3}x_n^3 - y_n + I_{\text{ext}} \\ \qquad\quad + k\tanh(\varphi_n)(x_n - x_{n-1}), \\ y_{n+1} = 0.1(ax_n + b) - 0.1y_n, \\ \varphi_{n+1} = \varphi_n + \kappa \cdot (x_n - w_n), \\ w_{n+1} = x_n. \end{cases} \tag{13}$$

To enable quantitative analysis of the dynamic characteristics (the FHN with one memristor and the coupled FHN systems), we provide dedicated pseudocode in Algorithms 2 and Algorithm 3. The core of this code transforms the coupled dynamical equations of the neuron and memristor into an iterative discrete-time computation process. By simultaneously solving the evolution of state variables and LEs, it enables quantitative characterization of the system's stability, bifurcation structure, and chaotic dynamics. With this pseudocode, the transition rules of neuronal firing patterns under memristive coupling can be accurately and quantitatively described, providing a single-neuron-level numerical verification tool for subsequent network-level dynamical analysis.

**Algorithm 2** DiscreteOneMemFHN model.

**Input:** $a$, $b$, $I_{\text{ext}}$, $k$, init, $N$.
**Output:** $x, y, w, q, C, Ly$.

Initialize $x, y, w, q, C$ (length $N$)
$x(1) = init(1), y(1) = init(2), w(1) = init(3), q(1) = init(4)$
$Q = 4 \times 4$ identity matrix, $ly_1 \sim ly_4 = 0$
**for** $i = 2$ to $N$ **do**
  $C(i) = k\tanh(q(i-1))(x(i-1) - w(i-1))$
  $x(i) = x(i-1) - x(i-1)^3/3 - y(i-1) + I_{\text{ext}} + C(i)$
  $y(i) = -0.1y(i-1) + 0.1(ax(i-1) + b)$
  $w(i) = x(i-1)$, $q(i) = q(i-1) + x(i-1) - w(i-1)$
  Compute Jacobian matrix $\boldsymbol{J}$ $(4 \times 4)$
  $[Q, R] =$ QR decomposition$(J \cdot Q)$
  $ly_1 \sim ly_4 +=$ log(abs$(R(1,1) \sim R(4,4))$)
**end for**
$Ly = [ly_1, ly_2, ly_3, ly_4]/(N-1)$

### 3.2. The coupled FHNs

This paper constructs a pair of neurons that achieve spike coupling through memristors. The first neuron follows the standard FHN model dynamics, while the second neuron is regulated by its membrane potential. The memristor connecting the two serves as a functional simulation unit for mimicking biological synapses. As a result, the coupled FHNs are defined by

$$\begin{cases} x_{1,n+1} = x_{1,n} - \dfrac{1}{3}x_{1,n}^3 - y_{1,n} + I_{\text{ext}}, \\ y_{1,n+1} = 0.1(ax_{1,n} + b) - 0.1y_{1,n}, \\ x_{2,n+1} = x_{2,n} - \dfrac{1}{3}x_{2,n}^3 - y_{2,n} + I_{\text{ext}} \\ \qquad\quad + k\tanh(\varphi_n)(x_{2,n} - x_{1,n}), \\ y_{2,n+1} = 0.1(ax_{2,n} + b) - 0.1y_{2,n}, \\ \varphi_{n+1} = \varphi_n + \kappa \cdot (x_{2,n} - x_{1,n}), \end{cases} \tag{14}$$

where $k$ is the coupling strength. The system architecture is shown in Fig. 6, and the pseudo-code for the relevant implementation process is presented in Algorithm 3.

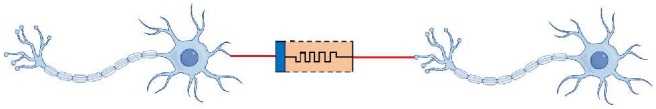


**Fig. 6.** The coupled FHNs with one memristor.

**Algorithm 3** Realization of the coupled FHNs model.

**Input:** $a$, $b$, $I_{\text{ext}}$, $k$, init, $N$
**Output:** $x1, y1, x2, y2, q, C, Ly$.

Initialize $x1, y1, x2, y2, q$ (length $N$), $C$ (length $N-1$)
$x1(1) = \text{init}(1)$, $y1(1) = \text{init}(2)$, $x2(1) = \text{init}(3)$, $y2(1) = \text{init}(4)$, $q(1) = \text{init}(5)$
$Q = 5 \times 5$ identity matrix, $ly_1 \sim ly_5 = 0$
**for** $i = 2$ to $N$ **do**
  $C(i-1) = k\tanh(q(i-1))(x2(i-1) - x1(i-1))$
  $x1(i) = x1(i-1) - x1(i-1)^3/3 - y1(i-1) + I_{\text{ext}}$
  $y1(i) = -0.1y1(i-1) + 0.1(ax1(i-1) + b)$
  $x2(i) = x2(i-1) - x2(i-1)^3/3 - y2(i-1) + I_{\text{ext}} + C(i-1)$
  $y2(i) = -0.1y2(i-1) + 0.1(ax2(i-1) + b)$
  $q(i) = q(i-1) + (x2(i-1) - x1(i-1))$
  Compute Jacobian matrix $\boldsymbol{J}$ $(5 \times 5)$
  $[Q, R] =$ QR decomposition$(J \cdot Q)$
  $ly_1 \sim ly_5 +=$ log(abs$(R(1,1) \sim R(5,5))$)
**end for**
$Ly = [ly_1, ly_2, ly_3, ly_4, ly_5]/(N-1)$

### 3.3. FHN network with ring coupling

To systematically investigate the impact of topology on the dynamics of memristive neural networks, this subsection constructs a ring coupling structure with regular connections using memristors, and then derives a small-world network through a random rewiring mechanism in the next subsection.

Here, as shown in Fig. 7, we set the number of neurons to 20, and each neuron is connected to two neurons on its left and right sides to construct a ring coupling. The mathematical model of the network is given by

$$\begin{cases} x_{i,n+1} = x_{i,n} - \dfrac{1}{3}x_{i,n}^3 - y_{i,n} + I_{\text{ext}}, \\ \qquad + \dfrac{k}{2M}\tanh(\varphi_{i,n})\left(2Mx_{i,n} - \sum\limits_{m=1}^{M} x_{i\pm m,n}\right), \\ y_{i,n+1} = 0.1\,(ax_{i,n}+b) - 0.1y_{i,n}, \\ \varphi_{i,n+1} = \varphi_{i,n} + 2Mx_{i,n} - \sum\limits_{m=1}^{M} x_{i\pm m,n}. \end{cases} \tag{15}$$

Therefore, the mathematical expression of the ring-coupled network exhibits the symmetry of local coupling. In this network, each neuron interacts only with the $M$ nearest neighbors on its left and right sides, respectively. This feature allows the basic memristive coupling effect to be clearly demonstrated without interference from a more complex topological structure.

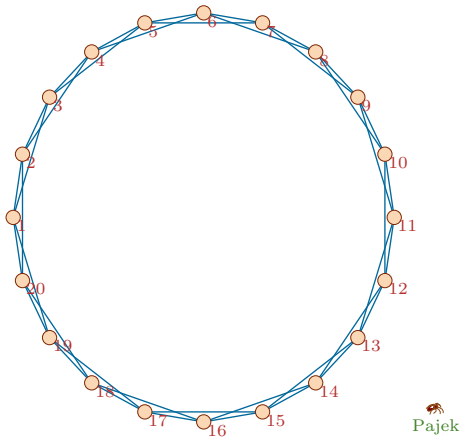



**Fig. 7.** FHN network with ring coupling.

Algorithm 4 is used to generate the adjacency matrix of the ring coupling: it creates an adjacency matrix $\boldsymbol{A}$ characterizing the ring topology (each node is only connected to its adjacent $k$ nodes) and writes it to a file.

**Algorithm 4** Ring network generation.

**Input:** Number of nodes $N$, Number of neighbors $K$.
**Output:** Adjacency matrix $\boldsymbol{A}$.

1: $A = \text{RingNetwork}(N,K)$ %Generate ring network
2: $\text{Writematrix}(A)$ % Write adjacency matrix to file

### 3.4. FHN network of small-world structure

While the ring coupling reveals the core mechanisms of memristive coupling, real neural systems typically feature a combination of local clustering and global connectivity.[44]

To better approximate biological realism, we introduce a small-world network structure, which is shown in Fig. 8. This topology retains local information processing capabilities while significantly shortening global communication distances through a small number of long-range connections, embodying the "low-cost, high-efficiency" optimization principle observed in biological neural networks.

Here, the small-world network is mathematically defined by

$$\begin{cases} x_{i,n+1} = x_{i,n} - \dfrac{1}{3}x_{i,n}^3 - y_{i,n} + I_{\text{ext}} \\ \qquad + \dfrac{k}{d_i}\tanh(\varphi_{i,n})\left(d_i \cdot x_{i,n} - \sum\limits_{j\in\mathcal{N}_i} x_{j,n}\right), \\ y_{i,n+1} = 0.1\,(ax_{i,n}+b) - 0.1y_{i,n}, \\ \varphi_{i,n+1} = \varphi_{i,n} + d_i \cdot x_{i,n} - \sum\limits_{j\in\mathcal{N}_i} x_{j,n}, \end{cases} \tag{16}$$

where $d_i$ is the degree of the $i$-th node, representing the number of connections to its neighboring nodes, and $\mathcal{N}_i$ denotes the set of neighbors of node $i$.

To construct and simulate discrete memristive FHN neural networks with a small-world network structure, this study provides corresponding pseudocodes. Algorithm 5 is used for small-world network generation, producing an adjacency matrix $\boldsymbol{A}$ that preserves local clustering characteristics while introducing long-range connections with probability $p$.

Algorithm 6 corresponds to the DiscreteNMemFHN model. After inputting the relevant parameters, it initializes node states and memristive variables, and realizes the dynamic evolution of the multi-neuron network through iterative computations. Finally, it outputs the node states and memristive coupling weights.

**Algorithm 5** Small-world network generation.

1: **function** SMALLWORLDNET($N,K,p$)
2: Initialize $N\times N$ sparse matrix $\boldsymbol{A}$ (all zeros). %Build initial ring topology
3: **for** $i = 1$ to $K/2$ **do**
4: $A$ += diagonal matrices with offset $i$ and $N-i$ (elements $= 1$)
5: **end for**
6: $A = A + A^T$. %Ensure undirected property
7: This_A $= A$. % Select nodes to rewire with probability $p$
8: StartVs $= \{$nodes where random$(0,1) < p\}$
9: **for** each $v_1 \in$ StartVs **do**
10: Find old neighbor $v_{2_\text{old}}$ of $v_1$ (valid connection, no self-loop, max $N$ tries)
11: Find new node $v_{2_\text{new}}$ for $v_1$ (no connection, no self-loop, max $N$ tries)
12: **if** $v_{2_\text{old}}$ and $v_{2_\text{new}}$ are valid **then**
13: Remove $(v_1, v_{2_\text{old}})$, add $(v_1, v_{2_\text{new}})$ (maintain symmetry)
14: **end if**
15: **end for**
16: $A =$ This_$A$ **return** $A$
17: **end function**

**Algorithm 6** DiscreteNMemFHN model.

**Input:** $M$, $a$, $b$, $I_{\text{ext}}$, $k$, $N$.
**Output:** $X, Y, W$.

$[mm, \sim] \leftarrow \text{size}(M)$, $W \leftarrow M$
Initialize $X, Y, Phi \in \mathbb{R}^{mm \times N}$ (node states)
$X(:,1), Y(:,1), Phi(:,1) \leftarrow \text{random}(mm, 1)$
**for** $i = 2$ to $N$ **do**
  **for** $j = 1$ to $mm$ **do**
    $index \leftarrow \text{find}(M(j,:) \neq 0)$, $Nod \leftarrow \text{length}(index)$
    $X(j,i) \leftarrow X(j,i-1) - X(j,i-1)^3/3 - Y(j,i-1) + I_{\text{ext}} + (k/Nod)\tanh(Phi(j,i-1))(Nod \cdot X(j,i-1) - \sum X(index, i-1))$
    $Y(j,i) \leftarrow -0.1Y(j,i-1) + 0.1(aX(j,i-1) + b)$
    $Phi(j,i) \leftarrow Phi(j,i-1) + (\sum X(index, i-1) - Nod \cdot X(j,i-1))$
    $W(j, index), W(index, j) \leftarrow \text{abs}((k/Nod)\tanh(Phi(j,i-1))(X(j,i-1) - X(index, i-1)))$
  **end for**
**end for**

These pseudocodes together form a complete toolchain for "topology generation–network simulation", providing support for studying the complex dynamics of discrete memristive neural networks.

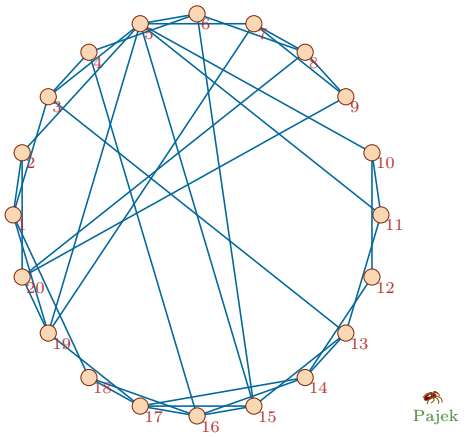



**Fig. 8.** A small world network with given number of nodes.

## 4. Performance analysis

### 4.1. Fixed points controlled dynamics

We define the function $z = x - x^3/3 + I_{\text{ext}}$, where $y$ is neglected due to its small magnitude relative to $I_{\text{ext}}$. Let $z = x$; the plots are shown in Fig. 9. It shows that the intersection point is the fixed point $x_o$ ($x_n = x_{n+1}$). The following observations are made:

(i) if $x_n < x_o$, then $x_{n+1} > x_n$,

(ii) if $x_n > x_o$, then $x_{n+1} < x_n$.

Regarding the intersection point $x_o$, take $x_n = x_{n+1} = x_o$ and $y_n = y_{n+1} = y_o$, then we have

$$\frac{1}{3}x_o^3 + \frac{ax_o + b}{11} - I_{\text{ext}} = 0. \tag{17}$$

Here, $x_o$ is related to the values of parameters $a$ and $b$.

As shown in Fig. 10, when $a$ takes 0.1 (periodic), 0.3 (chaotic), and 0.4 (chaotic), we present the time-series diagrams of $x_n$ and $x_o$. It is easy to verify that the graphs of $x_{n+1} = x_n - \frac{1}{3}x_n^3 - y_n + I_{\text{ext}}$ and $x_{n+1} = x_n$ have exactly one intersection point, indicating that the fixed point $x_o$ is unique. However, as $I_{\text{ext}}$ increases from 0 to 2, the system exhibits a phenomenon of transitioning from a single stable point to a double period, then to a quadruple period, and finally to chaos, as shown in Fig. 11.

Next, we determine the stability of the fixed point $x_o$.

Let $a = 0.4$ and $b = 0.3$ be the illustrative parameters. Thus, Eq. 17 transforms to

$$\frac{1}{3}x_o^3 + \frac{0.4x_o + 0.3}{11} - I_{\text{ext}} = 0. \tag{18}$$

Meanwhile, the Jacobian matrix of disFHN is

$$\boldsymbol{J} = \begin{bmatrix} 1 - x_o^2 & -1 \\ 0.04 & -0.1 \end{bmatrix}, \tag{19}$$

where $I_{\text{ext}}$ takes values in $[-2, 2]$.

Here, two specific scenarios with given values of $I_{\text{ext}}$ are presented:

(i) When $I_{\text{ext}} = 0$, $x_o = -0.3516$. Substituting into matrix $\boldsymbol{J}$, the eigenvalues are calculated as $\lambda_1 = 0.8446$ and $\lambda_2 = -0.0682$. Since the magnitudes of all eigenvalues satisfy $|\lambda_i| < 1$, this fixed point is stable.

(ii) When $I_{\text{ext}} = 1.2$, $x_o = 1.4970$, and the corresponding eigenvalues are $\lambda_1 = -1.2141$ and $\lambda_2 = -0.1269$. Because there exists an eigenvalue with $|\lambda_1| > 1$, this fixed point is unstable.

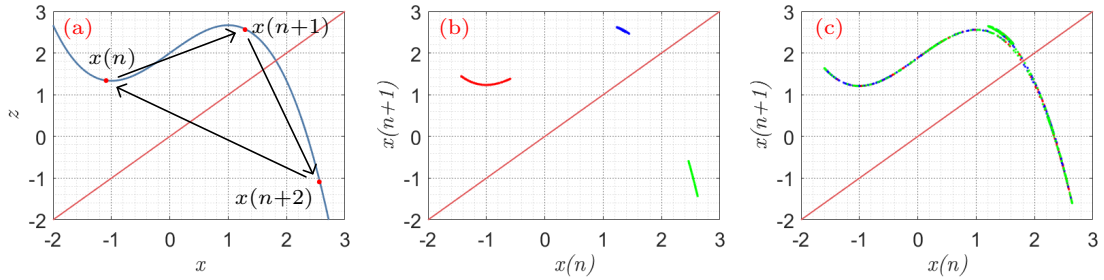



**Fig. 9.** Iteration map diagram of disFHN with $k = 0.01$, $b = 0.3$, $I_{\text{ext}} = 2.0$, and $z = x$. (a) $a = 0.1$, (b) $a = 0.3$, (c) $a = 0.4$.

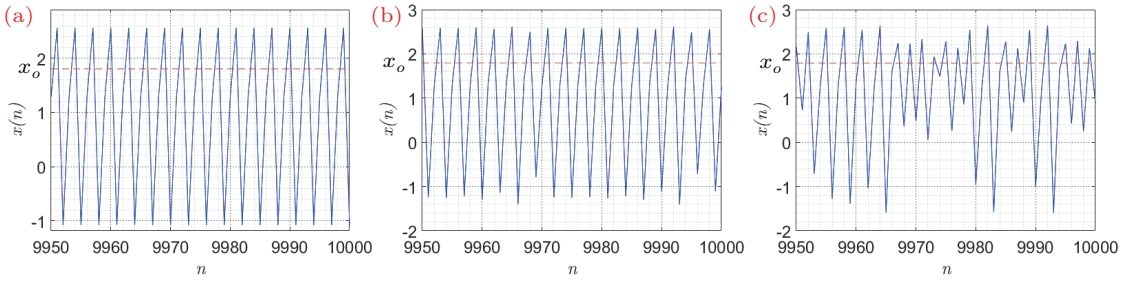



**Fig. 10.** The phase diagram of disFHN with $b = 0.3$, $k = 0.01$, and $I_{\text{ext}} = 2.0$. (a) $a = 0.1$, (b) $a = 0.3$, (c) $a = 0.4$.

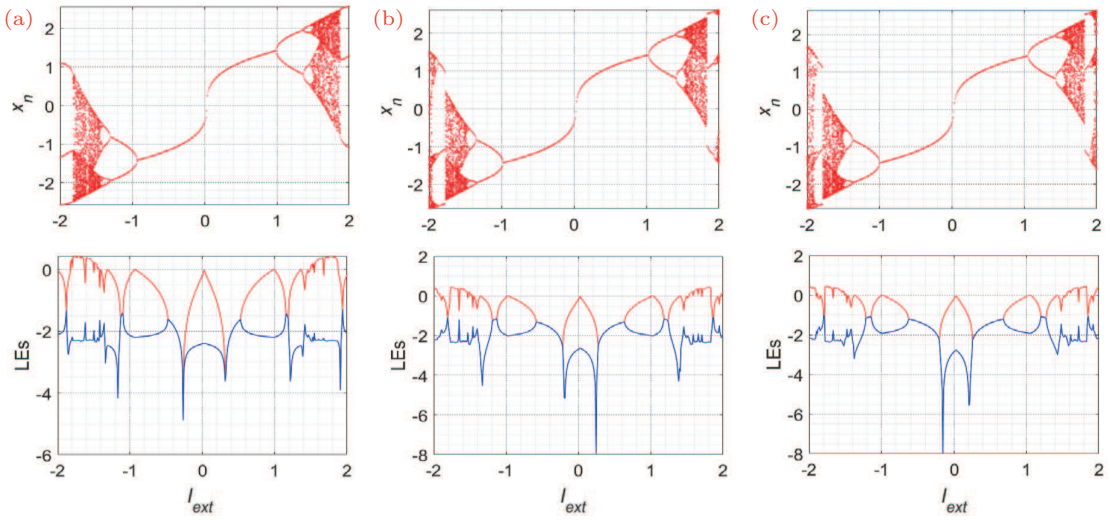



**Fig. 11.** The bifurcation and LEs of disFHN with $I_{\text{ext}}$ varying, $b = 0.3$, and $k = 0.01$. (a) $a = 0.1$, (b) $a = 0.3$, (c) $a = 0.4$.

Based on the bifurcation diagram of the discrete FHN system with respect to the parameter $I_{\text{ext}}$, we define the stability criterion: for a given $I_{\text{ext}}$, if the magnitudes of all eigenvalues of the Jacobian matrix are less than 1, the stability indicator (SI) outputs 1 (stable state); if there is at least one eigenvalue whose magnitude is greater than 1, the indicator (SI) outputs 0 (unstable state). That is

$$SI = \begin{cases} 1, & \text{if } \max_i |\lambda_i| < 1, \\ 0, & \text{otherwise}, \end{cases} \tag{20}$$

where $\lambda_i$ is the eigenvalue of the Jacobian matrix as given in Eq. 19.

The stability diagram of disFHN with respect to $I_{\text{ext}}$ is depicted in Fig. 12, which aligns with the bifurcation diagram. Upon reaching the fixed point, it is observed that $x_{n-1} = x_n = x_{n+1} = x_o$ and $y_n = y_{n+1}$. At this juncture, the self-coupling term $k\tanh(\varphi_n)[x_n - x_{n-1}]$ equals zero. Consequently, the DiscreteOneMemFHN model reduces to the disFHN model. Therefore, the determination of the fixed point in the DiscreteOneMemFHN model is completely consistent with that in the disFHN model and will not be repeated here.

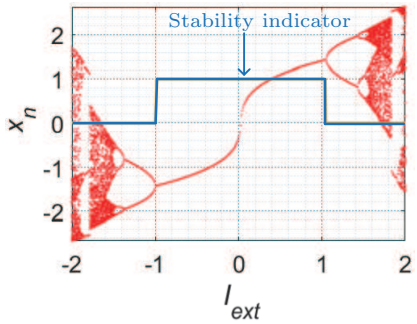



**Fig. 12.** Stability of disFHN with $I_{\text{ext}}$ varying, $a = 0.4$, $b = 0.3$, and $k = 0.01$. $SI = 1$ (stable), $SI = 0$ (unstable).

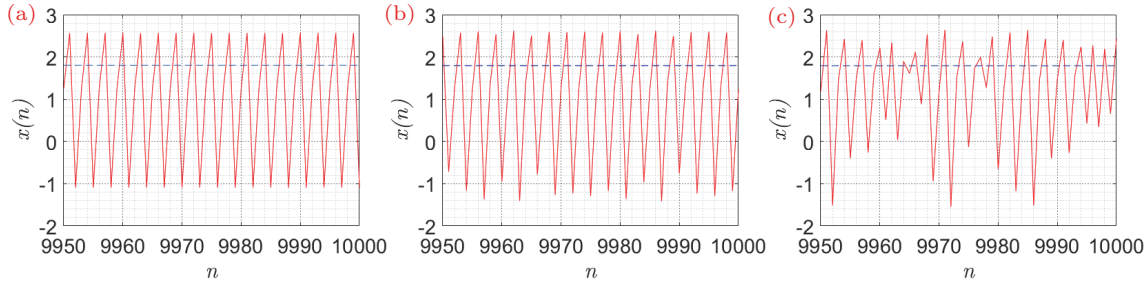



**Fig. 13.** The time series of DisOneMemFHN with $b = 0.3$, $k = 0.01$, and $I_{\text{ext}} = 2.0$. (a) $a = 0.1$, (b) $a = 0.3$, (c) $a = 0.4$.

The time series of DiscreteOneMemFHN are shown in Fig. 13.

To further validate the fixed point theory and comprehensively characterize the dynamical transitions in the discrete memristive FHN system, we systematically studied the phase diagram with respect to the key parameter $a$, as well as the bifurcation behavior of $k$ and the LE.

As depicted in Fig. 14(a) for $a = 0.1$, the system evolves on a stable periodic orbit. At $a = 0.3$ (Fig. 14(b)), the trajectory forms a complex, multi-loop structure that remains bounded but does not repeat, indicating a transition to aperiodic dynamics. For $a = 0.4$ (Fig. 14(c)), the trajectory further evolves into an irregular, bounded attractor characterized by a complex visitation pattern in phase space. Critically, the fixed point $x_o$ remains invariant and serves as a reference across all dynamical regimes — periodic, transitional, and chaotic — visually affirming its central role as proposed in the fixed point theory.

Figure 15 presents the phase-specific bifurcation diagrams and corresponding LE spectra for parameter $a$ varying from $-0.3$ to 0.6 with fixed coupling strength $k = 0.01$. The bifurcation diagrams for $x(3i+1)$, $x(3i+2)$, and $x(3i+3)$ reveal a clear period-3 structure in certain parameter regions, indicating the emergence of complex oscillatory patterns. Notably, the transition from periodic to chaotic behavior occurs around $a \approx 0.2$–$0.3$, which aligns with our previous stability analysis of the fixed point. The corresponding LE spectrum provides quantitative evidence for these dynamical transitions, with positive LEs in the region $a > 0.3$ confirming chaotic dynamics, and non-positive values for $a < 0.2$ indicating periodic or quasi-periodic behavior, thus demonstrating the robustness of the fixed point theory across different dynamical regimes.

Importantly, the dependence on memristive coupling strength $k$ (Fig. 16) reveals a counterintuitive regulatory mechanism: with increasing $k$, the system transitions from chaotic to periodic states, specifically entering a stable period-3 regime as evidenced by the negative LEs. This ordered state emergence underscores the suppressive role of memristive coupling in chaotic dynamics, effectively modulating neuronal synchronization patterns toward more regular oscillatory behavior. Such memristive control provides a mechanism for stabilizing neural activity through appropriate coupling strength tuning, further validating the theoretical framework established in our fixed point analysis.

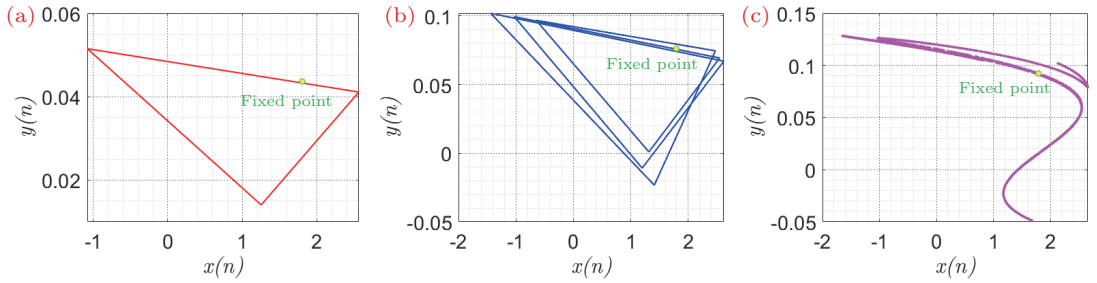



**Fig. 14.** The phase diagram of DisOneMemFHN with $b = 0.3$, $k = 0.01$, and $I_{\text{ext}} = 2.0$. (a) $a = 0.1$, (b) $a = 0.3$, (c) $a = 0.4$.

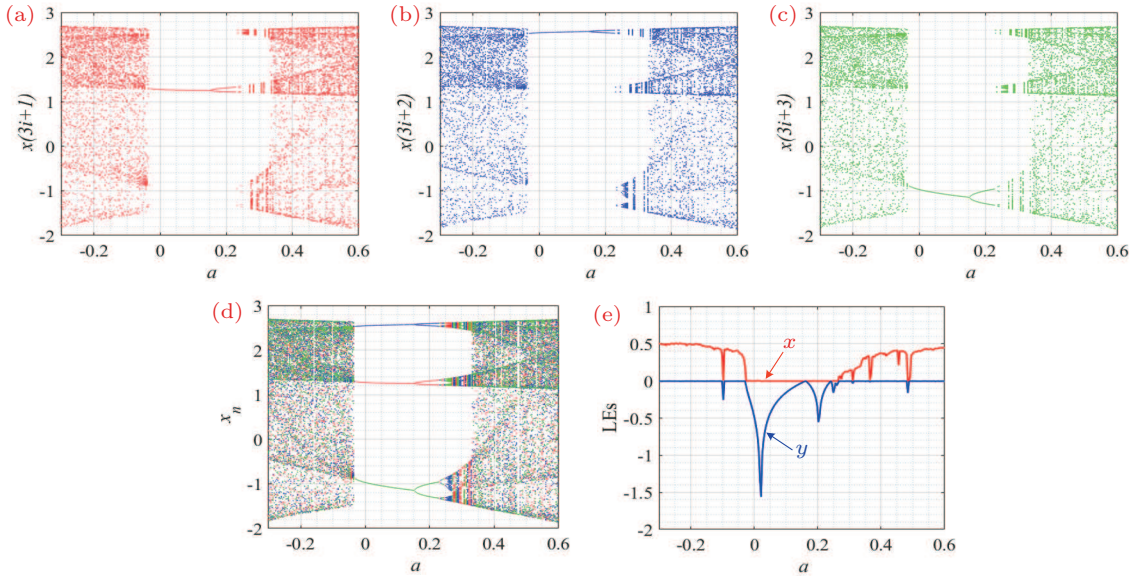



**Fig. 15.** The bifurcation and LEs of DisOneMemFHN with $a$ varying, $b = 0.3$, $k = 0.01$, and $I_{\text{ext}} = 2.0$. (a) $x(3i+1)$, (b) $x(3i+2)$, (c) $x(3i+3)$, (d) $x(n)$, (e) LEs.

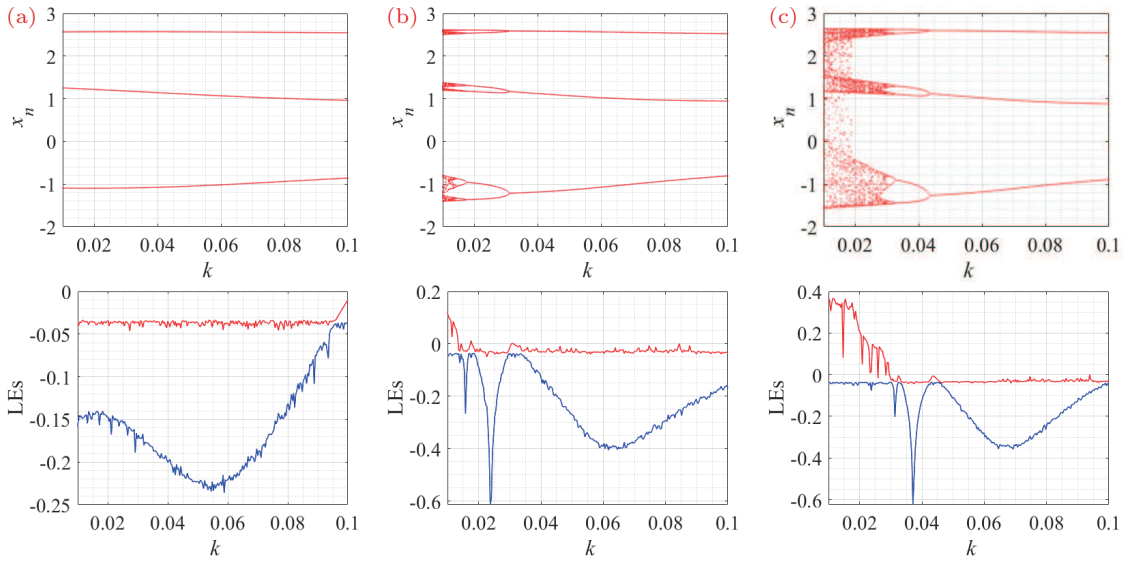



**Fig. 16.** The bifurcation and LEs of DisOneMemFHN with $k$ varying, $b = 0.3$, and $I_{\text{ext}} = 2.0$. (a) $a = 0.1$, (b) $a = 0.3$, (c) $a = 0.4$.

Furthermore, within the coupled FHN neurons, the segment comprising $x_1$ and $y_1$ (Neuron 1) constitutes the standard FHN neuron model, whereas $x_2$ (Neuron 2) is driven by Neuron 1 via a memristor. The fixed point for Neuron 2 must satisfy

$$\frac{1}{3}x_{2,o}^3 + \frac{ax_{2,o}+b}{11} + I_{\text{ext}} + k\tanh(\varphi_n)(x_{2,o}-x_{1,o}) = 0. \quad (21)$$

The key insight is recognizing that the coupling term

$$C = k\tanh(\varphi_n)(x_{2,o}-x_{1,o})$$

introduces a bounded perturbation to the fixed point equation. Since $\tanh(\varphi_n) \in (-1,1)$, the coupling term is constrained to

$$C \in [-k|x_{2,o}-x_{1,o}|,\ k|x_{2,o}-x_{1,o}|]. \quad (22)$$

This bounded perturbation translates to a corresponding range for $x_{2,o}$, which can be determined by solving the fixed point equation at the extremal values of $C$. The monotonic relationship between $C$ and $x_{2,o}$ ensures a well-defined range $[x_{2,\min}, x_{2,\max}]$. In this context, equation (21) becomes

$$\begin{cases} \dfrac{1}{3}x_{2,\max}^3 + \dfrac{ax_{2,\max}+b}{11} + I_{\text{ext}} + C_{\min} = 0, \\ \dfrac{1}{3}x_{2,\min}^3 + \dfrac{ax_{2,\min}+b}{11} + I_{\text{ext}} + C_{\max} = 0. \end{cases} \quad (23)$$

Here, the coupling term $C$ exhibits a monotonically decreasing relationship with respect to $x_{2,o}$.

### 4.2. Synchronization in the coupled FHNs

Simulations with parameters $a = 0.1$, $b = 0.3$, $I_{\text{ext}} = 2$, and $k = 0.01$ (where Neuron 1 is periodic) reveal two distinct scenarios for the coupled FHN neurons.

**Case 1:** As depicted in Figs. 17(a) and 17(b), the coupling term is in a three-periodic state. There is a stable phase difference between $x_2$ and $x_1$, satisfying $x_{1,i} \approx x_{2,i-1}$. From Fig. 17(a), we observe that the trajectories of $x_1$ and $x_2$ have a consistent oscillating pattern but with a noticeable phase shift. Fig. 17(b) shows that the coupling term varies periodically with two distinct frequency components, consistent with the double-periodic state description, reflecting the dynamic interaction that leads to the phase lag between the membrane potentials of the two neurons.

**Case 2:** When $\varphi_n = \varphi_{n+1}$, $C_{\min} = C_{\max} = 0$, and $x_{1,o} = x_{2,o}$, as shown in Figs. 17(c) and 17(d), the two neurons achieve complete synchronization. In Fig. 17(c), the trajectories of $x_1$ and $x_2$ almost overlap, indicating that their electrical activities are perfectly aligned. Fig. 17(d) illustrates that the coupling term rapidly diminishes to zero and stabilizes, indicating the absence of an effective coupling interaction between the neurons. In this case, the system behaves as two separate discrete FHN neuron models that maintain complete synchronization, highlighting a distinctive attribute of the system within the specified parameter regime.

For parameters $a = 0.3$, $b = 0.3$, $I_{\text{ext}} = 2$, and $k = 0.01$, $x_1$ exhibits a state of chaos. For the coupled FHN neurons in this study, let the discrete-time series of action potentials of the two neurons be $x_{1,n}$ and $x_{2,n}$ ($n = 1,2,\ldots,N$, where $N$ denotes the number of iteration steps). The derivation of the Phase Locking Value (PLV) is as follows.

**(i) Extraction of instantaneous phase:** Construct the analytic signal $X_{\text{analyt},k} = \text{hilbert}(x_{k,n})$ (for $k = 1,2$) via the Hilbert transform, and obtain the instantaneous phase by calculating the argument of the analytic signal, i.e.

$$\phi_{k,n} = \angle X_{\text{analyt},k},$$

where $\angle$ represents the argument operation of complex signals. This step is adapted to the discrete-time sequence characteristics of the system derived from Euler's algorithm (Eq. (11)).

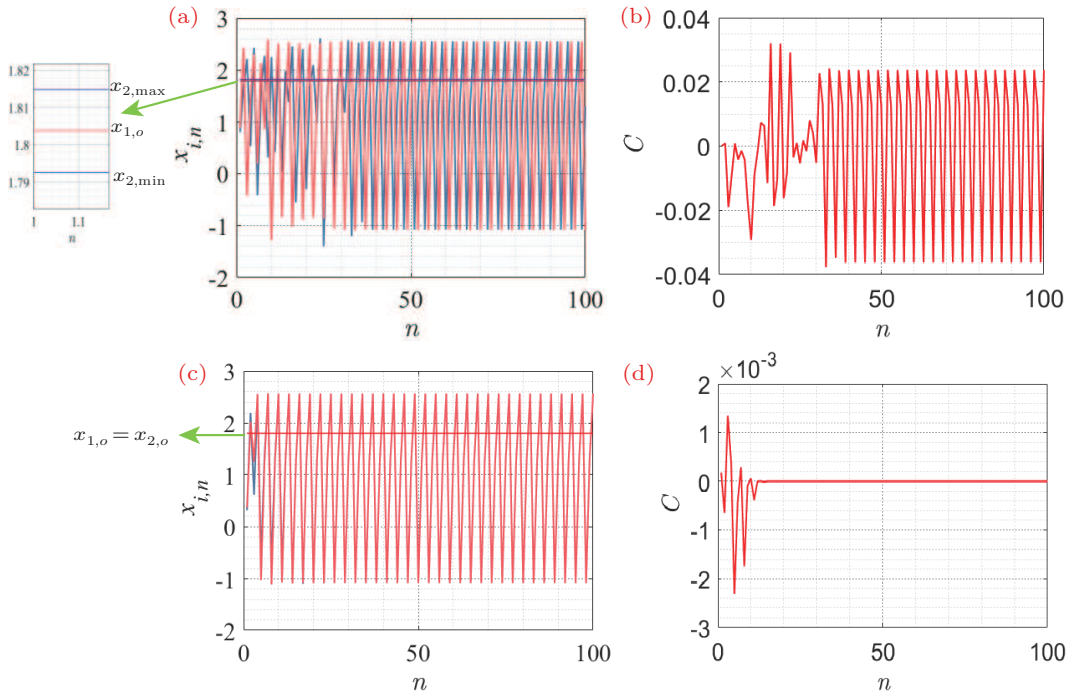



**Fig. 17.** The time series of coupled FHNs with $a = 0.1$, $b = 0.3$, $k = 0.01$, and $I_{\text{ext}} = 2.0$.

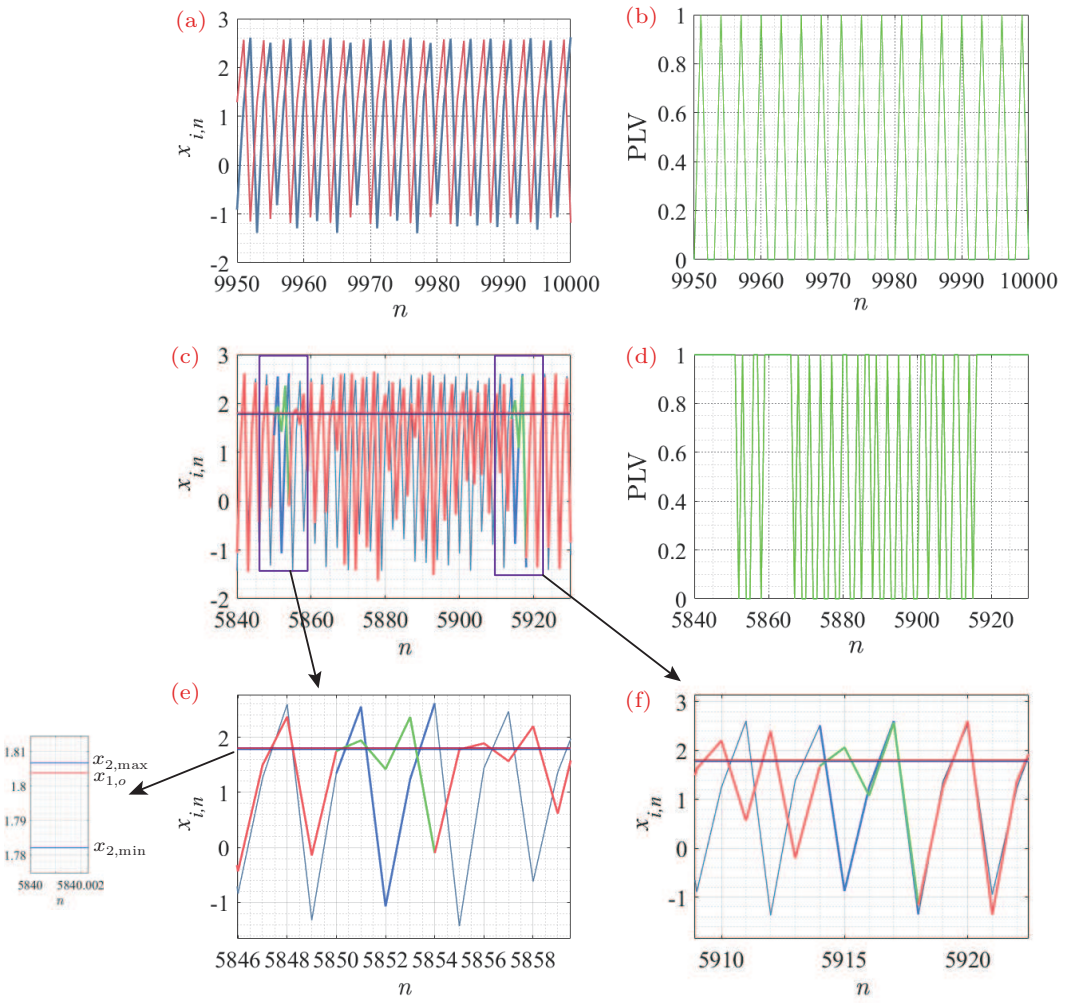



**Fig. 18.** The time series of coupled FHNs with $a = 0.3$, $b = 0.3$, $k = 0.01$, and $I_{\text{ext}} = 2.0$. (a) and (b) Case 1, (c) and (d) Case 2, (e) synchronization to desynchronization in phase, (f) desynchronization to synchronization in phase.

**(ii) Definition of phase difference:** Define the phase difference between the two neurons as

$$\Delta\phi_n = \phi_{1,n} - \phi_{2,n}.$$

**(iii) PLV calculation:** Quantify phase synchronization based on the average of complex exponentials, with the formula

$$\mathrm{PLV} = \left| \frac{1}{N} \sum_{n=1}^{N} \mathrm{e}^{\mathrm{j}\Delta\phi_n} \right|,$$

where $j$ is the imaginary unit and $|\cdot|$ denotes the complex modulus. The value of *PLV* ranges from 0 to 1: when *PLV* approaches 1, it indicates strong phase locking (synchronization) between neurons; when it approaches 0, it indicates phase decoupling (asynchronization), which matches the experimental observation of synchronization–desynchronization transitions in Fig. 18.

Two representative cases are as follows:

**Case 1:** There is a stable phase difference between neurons, and the PLV oscillates between 0 and 1, as shown in Figs. 18(a) and 18(b).

**Case 2:** The phase is initially desynchronized, then enters synchronization, and subsequently reverts to desynchronization, as shown in Figs. 18(c) and 18(d).

We examine the scenario depicted in Fig. 18(c), wherein the phase transitions from synchronized to desynchronized states and subsequently returns to synchronization, as illustrated in Figs. 18(e) and 18(f). When $a = 0.3$, $b = 0.3$, $k = 0.01$, and $I_{\mathrm{ext}} = 2.0$, although $x_1$ is in a weak chaotic state, it exhibits a three-period cycle (rise–rise–fall), but the phase of $x_2$ does not follow the peak pattern of $x_1$. According to Eqs. (17) and (23), we have $x_{1,o} = 1.7887$, $C_{\max} = 0.0104$, $C_{\min} = -0.0426$, $x_{2,\min} = 1.7812$, $x_{2,\max} = 1.8088$.

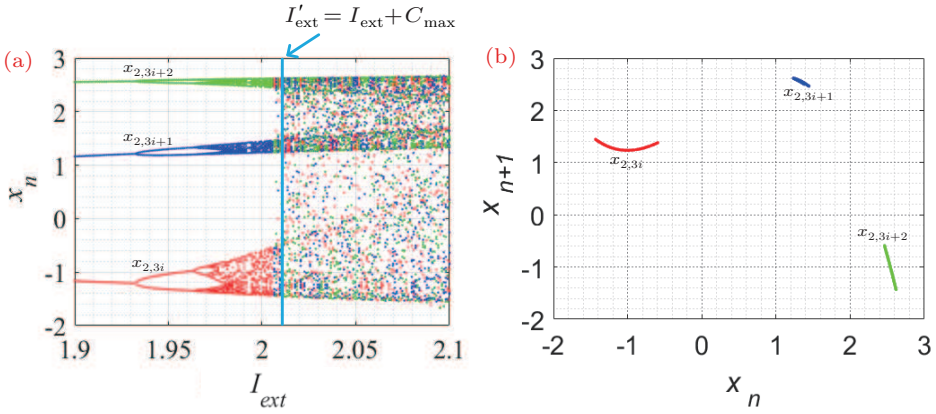



**Fig. 19.** (a) Bifurcation of disFHN with $I_{\mathrm{ext}}$ varying, and (b) phase diagram of disFHN with $a = 0.3$, $b = 0.3$, $k = 0.01$, and $I_{\mathrm{ext}} = 2.0$.

In Neuron 2, we can combine the coupling term $k\tanh(\varphi_n)(x_{2,n} - x_{1,n})$ and the stimulus current $I_{\mathrm{ext}}$ into a time-varying stimulus current $I'_{\mathrm{ext}}$. At this point, the model of Neuron 2 is a discrete FHN (disFHN) model with the time-varying stimulus current $I'_{\mathrm{ext}}$. Figure 19(a) shows the bifurcation diagram of the disFHN model in the vicinity of $I_{\mathrm{ext}} = 2$. When $I_{\mathrm{ext}} \leq 2$, $x_{2,3i}$, $x_{2,3i+1}$, and $x_{2,3i+2}$ $(i = 0, 1, \ldots)$ strictly concentrate in their respective three regions (red, blue, and green), as depicted in Fig. 19(b). When $I_{\mathrm{ext}}$ reaches a certain threshold (e.g., $I_{\mathrm{ext}} = 2.0 + \max(\mathrm{coupling})$), $x_{2,n}$ will appear in all regions (including red, blue, and green). Thus, there exists a case where $x_{2,i} < x_{2,o}$ and $x_{1,i} < x_{1,o}$, such that $x_{2,i+1} > x_{2,o} > x_{2,i}$ (membrane potential rises) and $x_{1,o} > x_{1,i+1} > x_{1,i}$ (membrane potential rises). Eventually, $x_{2,i+2} < x_{2,i+1}$ (membrane potential falls), and $x_{1,i+2} > x_{1,i+1}$ (membrane potential continues to rise). This causes $x_{2,n}$, which was originally in-phase (or out-of-phase) with $x_{1,n}$, to become out-of-phase (or in-phase).

Therefore, we can analyze that in the coupled FHNs model, when $a = 0.3$, $b = 0.3$, $k = 0.01$, and $I_{\mathrm{ext}} = 2.0$, there is no stable synchronization or stable phase difference in the phases of $x_{1,n}$ and $x_{2,n}$. As the iteration increases, the situation shown in Figs. 18(e) and 18(f) will repeatedly occur.

When $a = 0.4$, both $x_{1,n}$ and $x_{2,n}$ exhibit chaotic behavior, as shown in Fig. 20. It is noteworthy that even in this chaotic state, the theoretical framework remains valid. Although the state variables of the system are in chaotic oscillation, the core principles and analyses related to fixed points still hold. This indicates that in the coupled FHNs system under this parameter setting, the fixed point theory demonstrates good robustness — it is not only applicable to stable or periodic states but also to the analysis of chaotic states.

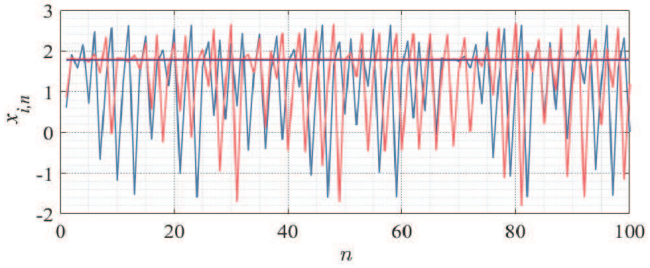



**Fig. 20.** Time series of the coupled FHNs with $a = 0.4$, $b = 0.3$, $k = 0.01$, and $I_{\mathrm{ext}} = 2.0$.

The synchronization dynamics between the two coupled

neurons are further elucidated in Fig. 21, which depicts both the internal state of Neuron 2 ($x_2$–$y_2$ plane, top row) and its relationship with Neuron 1 ($x_1$–$x_2$ plane, bottom row) for parameters $a = 0.1$, 0.3, and 0.4. The internal dynamics of Neuron 2, shown in the top row of Fig. 21, transition from a periodic orbit at $a = 0.1$ to a chaotic attractor at $a = 0.4$. At $a = 0.3$, the phase portrait exhibits a complex structure indicative of chaotic dynamics, albeit with a less extensive coverage of the phase space compared to $a = 0.4$.

The $x_1$–$x_2$ plots (bottom row) quantitatively reveal the synchronization regimes. For $a = 0.1$, the trajectory collapses onto the diagonal line ($x_1 = x_2$), confirming the state of complete synchronization between the two neurons, corresponding to Case 2 described in the text. At $a = 0.3$, the pattern diffuses into a complex, bounded cloud, signifying the breakdown of stable phase locking and the onset of intermittent synchronization, which aligns with the synchronization-desynchronization transitions observed in the time series and PLV analysis. Finally, for $a = 0.4$, the points spread widely, filling a broad region, which is characteristic of desynchronized chaotic dynamics.

To comprehensively characterize the coupled memristive FHN system, we focus on the second neuron ($x_2$) driven by memristive coupling, as the first neuron ($x_1$) follows standard discrete FHN dynamics previously established. Figure 22 shows the bifurcation diagram and LEs of $x_2$ versus parameter $a$ with $k = 0.01$. The choice of $k = 0.01$ is representative: lower $k$ values produce behaviors similar to isolated neurons, while $k = 0.02$ yields qualitatively comparable patterns, and $k \geq 0.03$ often leads to numerical divergence. Thus, $k = 0.01$ effectively captures memristive effects while ensuring stability. The bifurcation reveals periodic regimes ($a < 0.2$), transitional regions ($0.2 < a < 0.3$), and chaotic dynamics ($a > 0.3$), aligning with the above text.

Figure 23 examines $k$-dependence across $a$ values. At $a = 0.1$ (periodic), coupling modifies oscillations but maintains periodicity; at $a = 0.3$ (exhibiting complex dynamics), it induces state transitions; and at $a = 0.4$ (chaotic), it alters attractor structure without suppressing chaos. These results demonstrate how memristive coupling regulates dynamics across parameters.

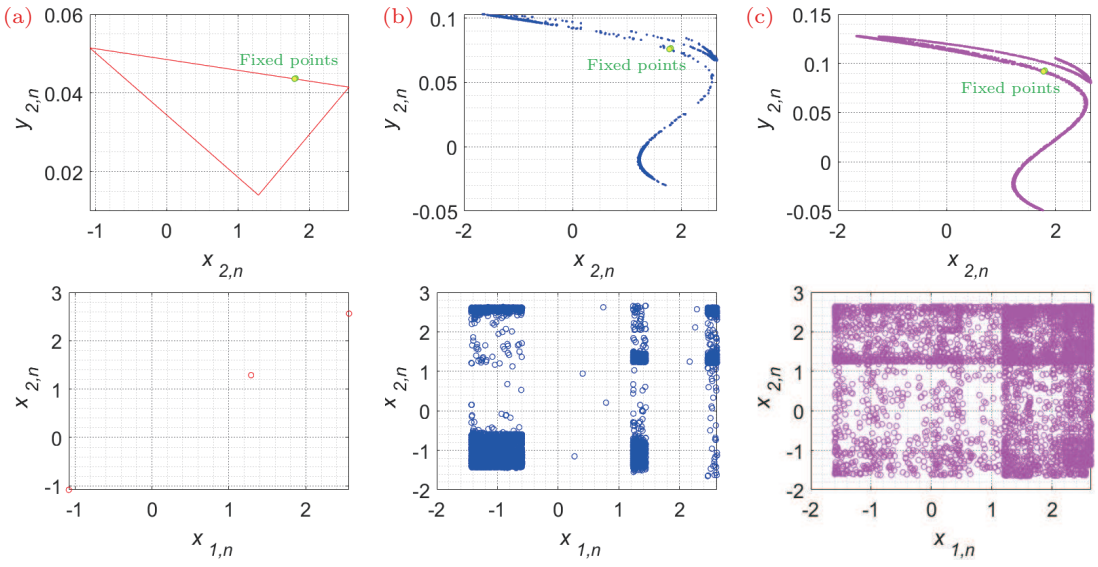



**Fig. 21.** Bifurcation diagram and LEs of $x_2$ in the coupled FHNs with $b = 0.3$, $k = 0.01$, and $I_{\text{ext}} = 2.0$ as $a$ varies.

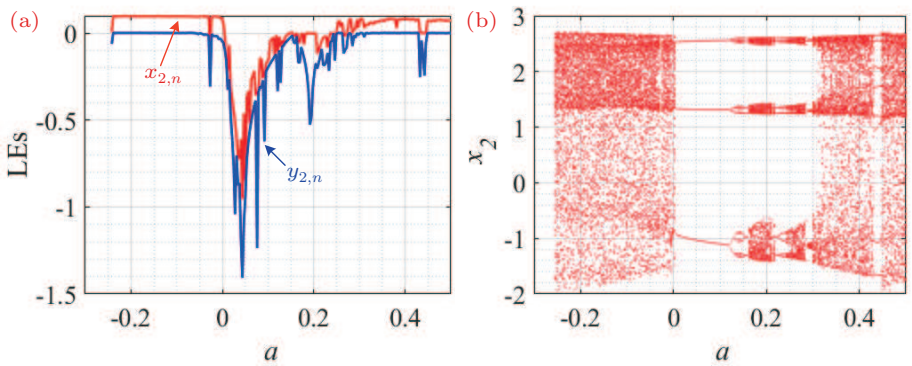



**Fig. 22.** Bifuraction and LEs of the coupled FHNs with $a$ varying, $b = 0.3$, $k = 0.01$, and $I_{\text{ext}} = 2.0$.

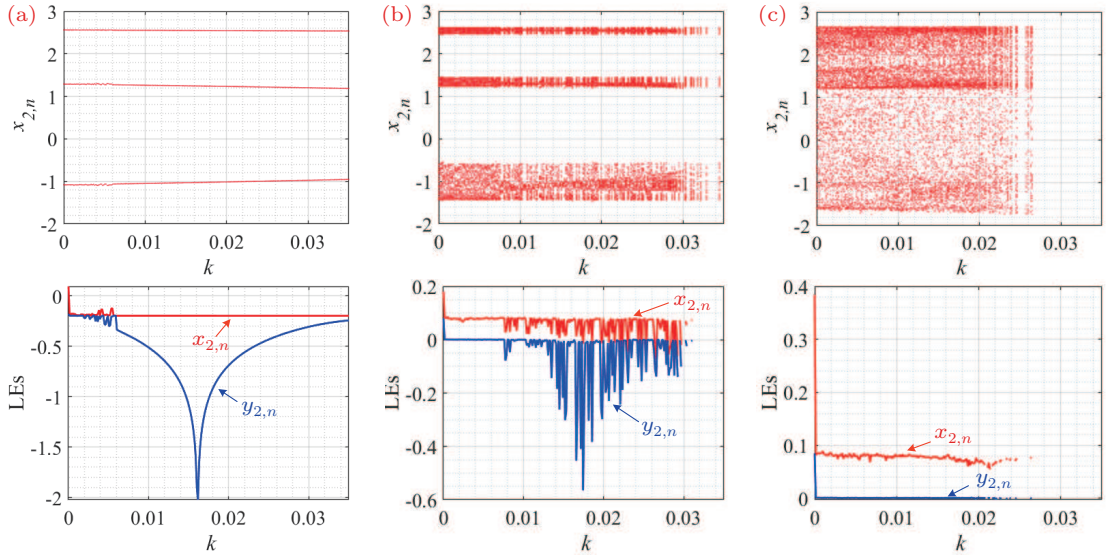



**Fig. 23.** Bifuraction and LEs of the coupled FHNs with $k$ varying, $b = 0.3$ and $I_{\text{ext}} = 2.0$. (a) $a = 0.1$, (b) $a = 0.3$, (c) $a = 0.4$.

### 4.3. Chimera states in the FHN network with ring structure

For $a = 0.1$, the network with ring structure does not manifest complete synchronization; instead, phase synchronization emerges in clusters, and as the iteration count $n$ increases, the system approaches a periodic state (refer to LEs $< 0$ for most neurons), as depicted in Fig. 24. In the computation of the fixed point $x_{i,o}$ for this system, the chosen coupling term is

$$C = \begin{cases} \max\left[\tanh(\varphi_{i,n})\left(4x_{i,n} - \sum_{m=1}^{2} x_{i\pm m,n}\right)\right], \\ \min\left[\tanh(\varphi_{i,n})\left(4x_{i,n} - \sum_{m=1}^{2} x_{i\pm m,n}\right)\right], \end{cases} \tag{24}$$

where $i = 1, 2, \ldots, 20$.

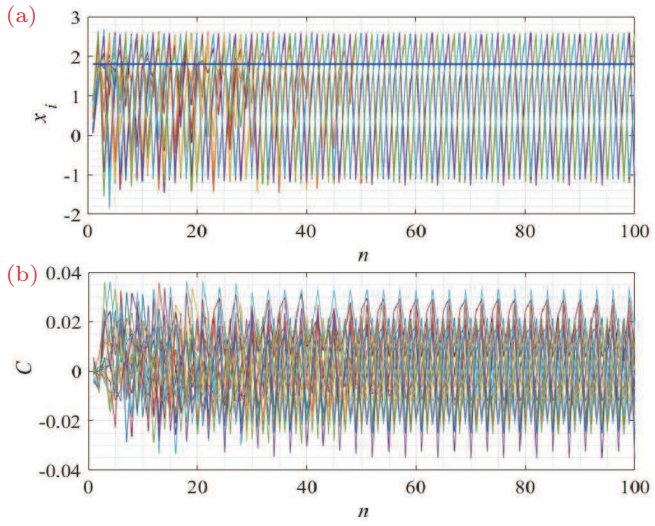



**Fig. 24.** (a) Trajectories and (b) coupling strength of ring coupling with $a = 0.1$, $b = 0.3$, $k = 0.01$, and $I_{\text{ext}} = 2.0$.

For the convenience of observation, we select nodes 1 to 5 for analysis. In the calculation of the fixed point $x_{i,o}$ here, $i$ in the selected coupling term takes values from 1 to 5. When $a = 0.3$, the phases of node 1 (blue) and node 3 (red) change from desynchronization to synchronization. This behavior is similar to that observed when $a = 0.3$ in the coupled FHNs and will not be repeated here. When $a = 0.4$, the system enters a chaotic state, but the theory regarding the fixed point still holds, as shown in Fig. 25.

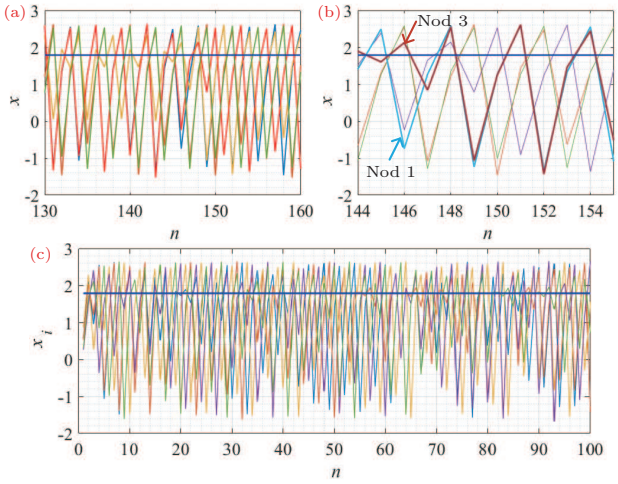



**Fig. 25.** Times series of ring coupling with $b = 0.3$, $k = 0.01$, and $I_{\text{ext}} = 2.0$. (a) $a = 0.3$, (b) desync-to-sync transition in phase, (c) $a = 0.4$.

Given the above nodal behavior (the coexistence of synchronous and asynchronous dynamics), we identify this as a chimera state. We present the coupling strength between nodes, the iteration values of each node, as well as LEs and bifurcation diagrams varying with $a$, as shown in Figs. 26 and 27.

The figures in Fig. 27 are organized in descending order, corresponding to $a = 0.1$, 0.3, and 0.4, respectively. These figures illustrate the interplay between the network coupling matrix and the spatiotemporal dynamics of chimera states. As

observed in Figs. 26 and 27, when $a = 0.1$ or $a = 0.3$, the entire network exhibits a chimera state. In this regime, different neuronal nodes simultaneously display both phase synchronization and asynchrony. Conversely, when $a = 0.4$, the chimera state breaks down, and the system transitions into a chaotic regime.

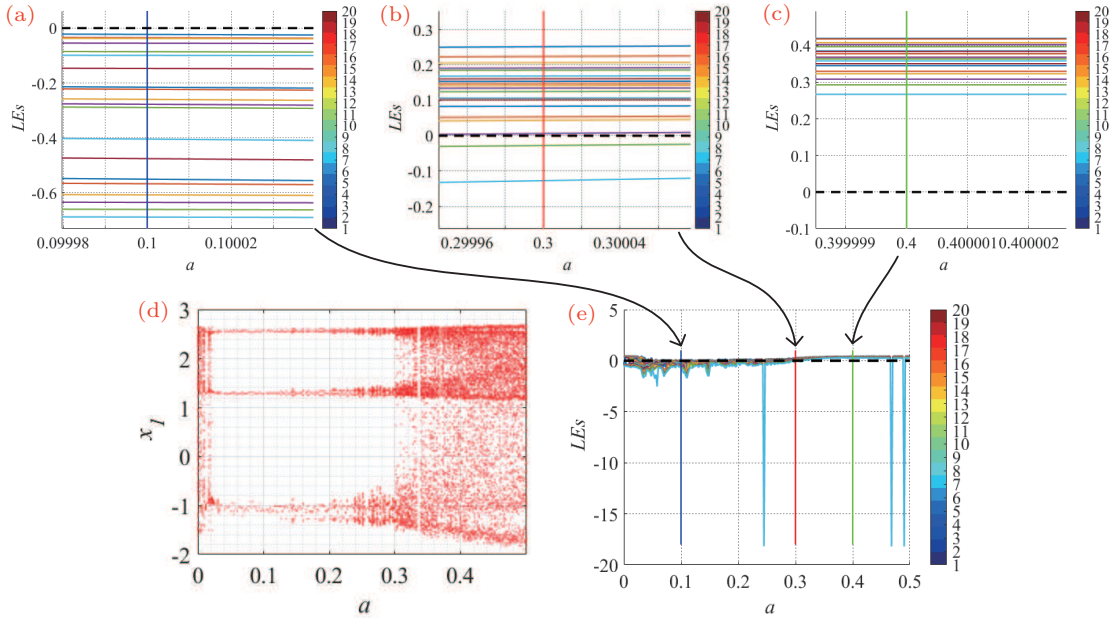



**Fig. 26.** Bifuraction and LEs of ring coupling with $b = 0.3$, $k = 0.01$, and $I_{\text{ext}} = 2.0$. (a) LEs with $a = 0.1$, (b) LEs with $a = 0.3$, (c) LEs with $a = 0.4$, (d) bifuraction of node 1, (e) LEs of ring coupling.

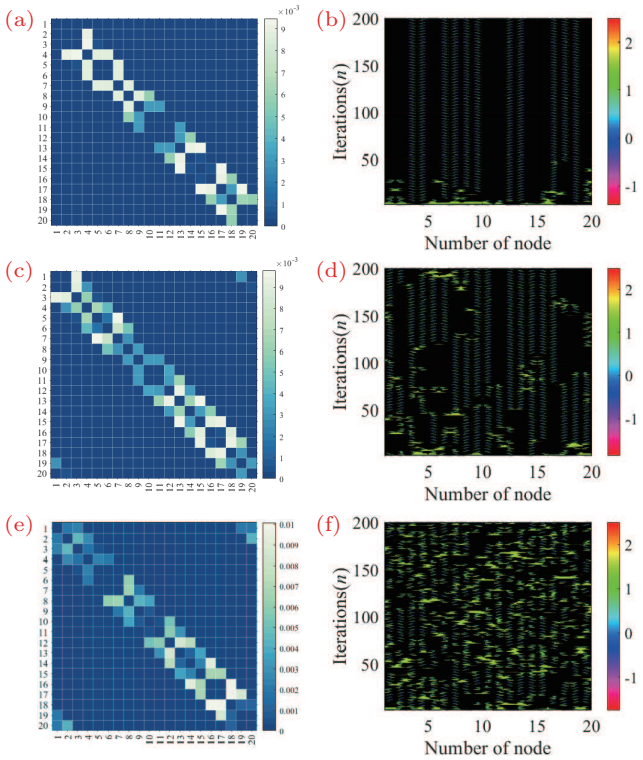



**Fig. 27.** Coupling strength matrix and chimera state in ring coupling with $b = 0.3$, $k = 0.01$, and $I_{\text{ext}} = 2.0$. (a) and (b) $a = 0.1$, (c) and (d) $a = 0.3$, (e) and (f) $a = 0.4$.

### 4.4. Local high-coupling clusters in small-world network

Starting from the ring-coupled network, we rewire connections between nodes with a probability of $p = 0.8$. This reconnection procedure modifies the initial regular topology of the ring structure, introducing a degree of randomness while preserving elements of the original connectivity. The elevated reconnection probability of $p = 0.8$ implies that most nodes will form new connections extending beyond the conventional ring structure, potentially yielding a topology resembling a small-world or random network. Such alterations to the network's structure are anticipated to exert a substantial influence on the network's dynamical behavior, including the genesis and evolution of chimera states.

The small-world network retains local high-coupling clusters (for example, node 5) and exhibits random long-range shortcuts (such as node 3 and node 13), combining the clustering property of the ring structure with the short-path characteristic of the small-world network. When $a = 0.1$ and $a = 0.3$, the network shows a chimera state with coexisting synchronous clusters and asynchronous regions, with an increase in $a$ reducing the synchronous region. When $a = 0.4$, the chimera state disappears, and the system fully enters a chaotic state, as shown in Fig. 28. The observed chimera states can be attributed to memristive heterogeneity-induced symmetry breaking. Although all neurons share identical parameters, the history-dependent memristive states $\varphi_{i,n}$ create effective heterogeneity through the state-dependent coupling $k\tanh(\varphi_{i,n})$. This dynamic heterogeneity enables the coexistence of coherent and incoherent clusters: neurons with similar memristive states tend to synchronize, forming coherent domains, while those with divergent memristive states remain incoherent. This mechanism aligns with established chimera

theory,[50,51] where symmetry breaking — whether through parameter heterogeneity or, in our case, dynamic state heterogeneity — underpins the formation of coexisting coherent and incoherent domains. The modulation of chimera patterns in small-world networks further demonstrates how topological constraints interact with this memristive symmetry-breaking mechanism.

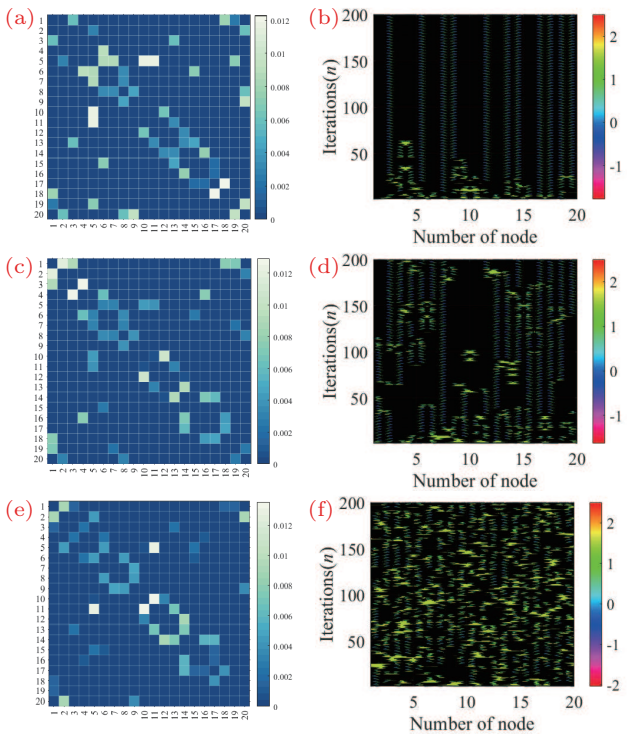



**Fig. 28.** Coupling strength matrix and the chimera state in small-world network with $b = 0.3$, $k = 0.01$, and $I_{\text{ext}} = 2.0$. (a) and (b) $a = 0.1$, (c) and (d) $a = 0.3$, (e) and (f) $a = 0.4$.

To address the potential influence of small-world rewiring probability on network dynamics, we systematically varied the parameter $p$ from 0.01 to 0.8. Interestingly, the fundamental dynamical regimes remained qualitatively similar across this parameter range: for $a = 0.1$ and $a = 0.3$, the network consistently exhibited clustered synchronization and chimera states, while for $a = 0.4$, chimera states dissolved into chaotic dynamics regardless of the specific $p$ value. This robustness suggests that the emergence of chimera states in our discrete memristive FHN network is primarily governed by the intrinsic neuronal dynamics and memristive coupling, with network topology playing a secondary role in modulating the spatial organization rather than determining the fundamental dynamical classes.

## 5. FPGA implementation

### 5.1. Implementation methodology

The primary objective of the FPGA implementation is to provide functional validation of the proposed mathematical models, confirming their realizability on digital hardware. The implementation was carried out on a Xilinx Artix-7 FPGA (XC7A200T-1FBG676C) platform, utilizing the Xilinx Vivado Design Suite for design entry, synthesis, and implementation.

A high-level architectural diagram of the implemented discrete FHN is shown in Fig. 29. The design directly reflects the mathematical formulation of the discrete FHN model. The core of the system consists of dedicated compute units for the neuron state variables ($x_n$, $y_n$). These compute units are implemented as combinational logic blocks that perform the iterative calculations defined by the discrete equations. The arithmetic operations within these units are realized using the FPGA's logic resources and built-in DSP slices. Double-precision floating-point arithmetic is employed throughout to ensure numerical accuracy consistent with software simulations, prioritizing model verification over hardware optimization.

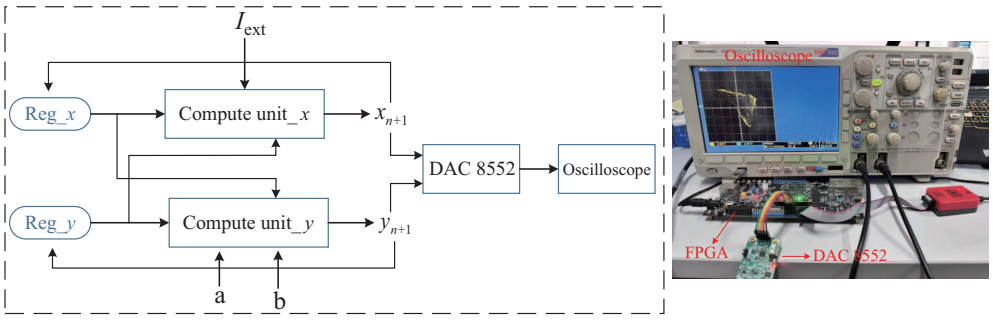



**Fig. 29.** Architecture and experimental platform of the FPGA implementation for the discrete FHN.

The iterative nature of the discrete-time system is managed by a synchronous state machine that controls data flow between compute units and registers at each time step $n$. The output values $x_{n+1}$ and $y_{n+1}$ are converted to analog signals via a DAC8552 digital-to-analog converter for real-time visualization on an oscilloscope, enabling direct comparison with numerical simulation results.

### 5.2. Numerical validation on hardware

The FPGA implementation successfully reproduces the rich dynamics observed in software simulations. Fig. 30 confirms the chaotic attractor of the discrete FHN system at $a =$

0.4, with its phase portrait and aperiodic time series closely matching the numerical results presented in Fig. 30.

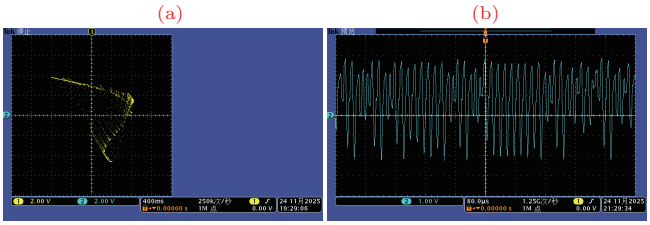



**Fig. 30.** FPGA implementation of disFHN at $a = 0.4$, $b = 0.3$, and $I_{\text{ext}} = 2.0$. (a) phase portrait in $x$-$y$ plane, (b) time series of $x_n$.

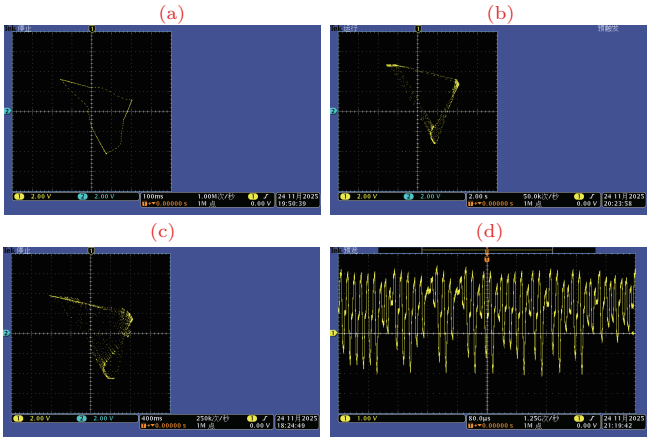



**Fig. 31.** FPGA implementation of DisOneMemFHN: Phase portraits for (a) $a = 0.1$, (b) $a = 0.3$, (c) $a = 0.4$. Parameters: $b = 0.3$, $I_{\text{ext}} = 2.0$, $k = 0.01$.

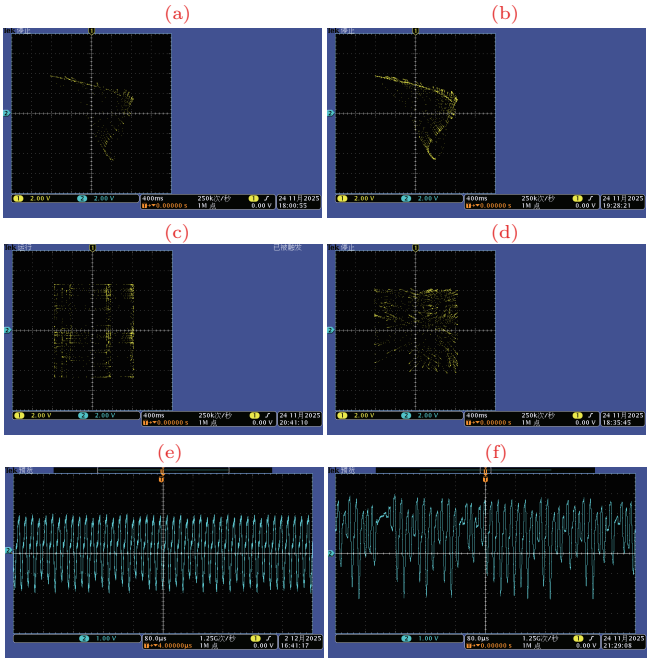



**Fig. 32.** FPGA implementation of the coupled FHNs: $x_2$–$y_2$ phase portraits with $b = 0.3$, $I_{\text{ext}} = 2.0$, $k = 0.01$ (a) $a = 0.3$, (b) $a = 0.4$, $x_1$–$x_2$ synchronization plots for (c) $a = 0.3$, (d) $a = 0.4$, time series for (e) $a = 0.3$, (f) $a = 0.4$.

For the DisOneMemFHN system, the FPGA results (Fig. 31) qualitatively reproduce the full dynamical transition governed by the parameter $a$, ranging from periodicity ($a = 0.1$) through transitional chaos ($a = 0.3$) to fully developed chaos ($a = 0.4$), as previously analyzed in Subsection 4.1.

The synchronization dynamics of the coupled FHN system were also faithfully captured on hardware. As shown in Fig. 32, the $x_1$–$x_2$ synchronization plots for $a = 0.3$ and $a = 0.4$ exhibit intermittent synchronization and desynchronized chaotic dynamics, respectively, consistent with their numerical counterparts, confirming the analyses in Subsection 4.2.

The visual fidelity of all implemented systems under high-precision floating-point arithmetic confirms that the proposed models can be faithfully executed on digital hardware. This successful hardware validation establishes the principal feasibility of deploying the proposed discrete memristive FHN networks on digital platforms, paving the way for their use in real-time, brain-inspired computing applications.

## 6. Conclusion

This study establishes a unified framework for discrete memristive FHN networks, linking nonlinear dynamics to neuromorphic applications. Three key contributions are highlighted.

First, a discrete memristor with tanh nonlinearity is introduced and integrated into FHN neurons, enabling the modeling of systems ranging from a single FHN neuron to ring and small-world networks.

Second, stability and bifurcation analyses reveal that the parameter $a$ governs transitions from periodic to chaotic dynamics. Memristive coupling induces diverse synchronization patterns, including phase-locking and synchronization–desynchronization transitions. The identification of a persistent fixed point — which organizes network activity across all regimes — provides a theoretical anchor. Physically, the history-dependent memristive coupling emulates synaptic plasticity, breaks symmetry, and explains the emergence and topology-dependent modulation of chimera states.

Third, FPGA implementation validates all models, confirming hardware feasibility for real-time applications.

In summary, this work bridges nonlinear theory with physical mechanisms such as stability and adaptive coupling. The fixed point theory offers practical control levers: (1) adjusting $I_{\text{ext}}$ stabilizes fixed points and tunes computational dynamics; (2) modulating the coupling strength $k$ directs synchronization behaviors, as demonstrated in our bifurcation and synchronization analyses. These principles provide a roadmap for parameter-guided design of future neuromorphic networks. Future work may explore diverse memristor nonlinearities, time-delay effects, and applications in secure communication and brain-inspired computing.

## Acknowledgments

This project was supported by the Natural Science Foundation of China (Grant Nos. 62501516, 61901530, 62071496, and 62061008), the Natural Science Foundation of Hunan Province (Grant No. 2020JJ5767), and the Natural Science Foundation of Hunan Province (Grant No. 2025JJ50391).

## References

[1] Chua L 1971 *IEEE Trans. Circuit Theory* **18** 507
[2] Strukov D B, Snider G S, Stewart D R, *et al.* 2008 *Nature* **453** 80
[3] Itoh M and Chua L O 2008 *Int. J. Bifurcation Chaos* **18** 3183
[4] Radwan A G and Fouda M E 2015 *On the Mathematical Modeling of Memristor, Memcapacitor, and Meminductor* Vol. 26 (Springer)
[5] Yang S, Kim T, Kim S, *et al.* 2023 *Nanoscale* **15** 13239
[6] Shelby R M, Burr G W, Boybat I, *et al.* 2015 *IEEE Int. Reliab. Phys. Symp.* pp 6A.1.1
[7] Pershin Y V and Di Ventra M 2010 *Neural Netw.* **23** 881
[8] Adhikari S P, Yang C, Kim H, *et al.* 2012 *IEEE Trans. Neural Netw. Learn. Syst.* **23** 1426
[9] Hodgkin A L and Huxley A F 1952 *J. Physiol.* **117** 500
[10] FitzHugh R 1961 *Biophys. J.* **1** 445
[11] Nagumo J, Arimoto S and Yoshizawa S 1962 *Proc. IRE* **50** 2061
[12] Yan B, He S and Wang S 2020 *Math. Probl. Eng.* **2020** 2468134
[13] He S, Sun K, Peng Y and Wang L 2020 *AIP Adv.* **10** 015332
[14] Muthuswamy B and Chua L O 2010 *Int. J. Bifurcation Chaos* **20** 1567
[15] You Y, Tian J and Tu J 2023 *Commun. Nonlinear Sci. Numer. Simul.* **125** 107405
[16] He S, Zhan D, Wang H, *et al.* 2022 *Entropy* **24** 786
[17] Deng Q, Wang C, Yang G, *et al.* 2025 *IEEE Internet Things J.* **12** 25559
[18] He S, Liu J, Wang H, *et al.* 2023 *Neurocomputing* **523** 1
[19] Zhang T, Yang K, Xu X, *et al.* 2019 *Phys. Status Solidi Rapid Res. Lett.* **13** 1900029
[20] Chang H, Li Y, Yuan F, *et al.* 2019 *Int. J. Bifurcation Chaos* **29** 1950086
[21] Fan Y, Huang X, Wang Z, *et al.* 2018 *Nonlinear Dyn.* **93** 611
[22] Yan X, Li Z and Li C 2024 *Chin. Phys. B* **33** 028705
[23] Xiao M, Zheng W X, Jiang G, *et al.* 2021 *IEEE Trans. Neural Netw. Learn. Syst.* **32** 1974
[24] Wang L, Shen Y, Yin Q, *et al.* 2015 *IEEE Trans. Neural Netw. Learn. Syst.* **26** 2033
[25] Duan S, Hu X, Dong Z, *et al.* 2015 *IEEE Trans. Neural Netw. Learn. Syst.* **26** 1202
[26] Zhang J and Liao X 2017 *AEU - Int. J. Electron. Commun.* **75** 82
[27] Guo Y, Ma J, Zhang X, *et al.* 2024 *Sci. China Tech. Sci.* **67** 1567
[28] Ma M, Yuan Z, Kalsoom U, *et al.* 2025 *Chin. Phys. B* **34** 100502
[29] Ma M L, Xie X H, Yang Y, Li Z J and Sun Y C 2023 *Chin. Phys. B* **32** 058701
[30] Lu J, Xie X, Lu Y, Wu Y, Li C and Ma M 2024 *Chin. Phys. B* **33** 048701
[31] Wu W, Wang M and Yang Q 2025 *Chin. Phys. B* **34** 050503
[32] Mou J, Cao H, Zhou N and Cao Y 2024 *IEEE Trans. Cybern.* **54** 7333
[33] Xu Q, Fang Y, Feng C, Parastesh F, Chen M and Wang N 2024 *Nonlinear Dyn.* **112** 13451
[34] Zhang X, Wang W, Liu Q, *et al.* 2018 *IEEE Electron Device Lett.* **39** 308
[35] Sboev A, Vlasov D, Rybka R, *et al.* 2021 *Math.* **9** 3237
[36] Jing Y and Xian Y 2024 *Proc. 2024 Prognostics and System Health Management Conf. (PHM)* pp 1–7
[37] Njitacke Z T, Awrejcewicz J, Telem A N K, *et al.* 2023 *IEEE Trans. Circuits Syst. II Express Briefs* **70** 791
[38] Rontogiannis A and Provata A 2021 *Eur. Phys. J. B* **94** 97
[39] Buzsáki G and Draguhn A 2004 *Science* **304** 1926
[40] Liang H, Cheng H, Wei J, *et al.* 2019 *IEEE Trans. Emerg. Top. Comput. Intell.* **3** 15
[41] Kuznetsov Y A 1998 *Elements of Appl. Bifurcation Theory* (Springer)
[42] Strogatz S H 2001 *Nonlinear Dyn. and Chaos* (Westview Press)
[43] Li Y, Lv M, Ma J, *et al.* 2024 *Nonlinear Dyn.* **112** 7541
[44] Deng Y and Li Y 2021 *Nonlinear Dyn.* **104** 4601
[45] Yu Y, Adu K, Tashi N, Anokye P, Wang X and Ayidzoe M A 2020 *IEEE Access* **8** 72727
[46] Chen C, Min F, Cai J and Bao H 2024 *IEEE Trans. Circuits Syst. I Regul. Papers* **71** 2308
[47] Lei Z and Ma J 2025 *Chaos* **35** 023158
[48] Zhan F and Liu S 2019 *Nonlinear Dyn.* **97** 2675
[49] Sporns O and Kotter R 2004 *PLoS Biol.* **2** e369
[50] Panaggio M J and Abrams D M 2015 *Nonlinearity* **28** R67
[51] Hizanidis J, Kouvaris N E, Zamora-López G, Díaz-Guilera A and Antonopoulos C G 2016 *Sci. Rep.* **6** 19845